Incremental Construction of the Unit 10 Peridotite, Rum Eastern Layered Intrusion, NW Scotland

Luke N. Hepworth[1*], Brian O'Driscoll[1, 2*], Ralf Gertisser[1], J. Stephen Daly[3,4] and C. Henry Emeleus[5]

[1]*School of Geography, Geology, and the Environment, Keele University, Keele ST5 5BG, UK*
[2]*School of Earth, Atmospheric and Environmental Science, University of Manchester, Oxford Road, Manchester M13 9PL, UK;*
[3]*UCD School of Earth Sciences and UCD Earth Institute, University College Dublin, Belfield, Dublin 4, Ireland*
[4]*Irish Centre for Research in Applied Geosciences, Belfield, Dublin 4, Ireland*
[5]*Department of Earth Sciences, Durham University, Science Labs, South Road, Durham DH1 3LE, UK*

[*]Corresponding authors: l.n.hepworth@keele.ac.uk, brian.odriscoll@manchester.ac.uk

ABSTRACT

The Rum Eastern Layered Intrusion (ELI) is the product of part of a ~60 Ma open-system magma chamber. The 16 coupled peridotite/troctolite ± gabbro macro-rhythmic units it contains represent crystallisation of multiple batches of basaltic and picritic magma. Within the ELI, Unit 10 has been considered the type example of batch fractionation of magma on Rum for more than 50 years, successively producing peridotite, troctolite and olivine gabbro. Detailed field observations and logs of the Unit 10 peridotite cumulate are presented here, together with mineralogical and textural analyses of Cr-spinel seams and their peridotite host rocks. Numerous harrisite layers are commonly associated with diffuse, laterally discontinuous platinum-group element (PGE) enriched Cr-spinel seams. Multiple millimetre–centimetre thick Cr-spinel seams occur at the bases, tops and within harrisite layers. These relationships are inconsistent with simple batch fractionation of magma. Critically, the harrisite layers also exhibit centimetre to metre-scale, upward oriented apophyses that point to injection of magma into the overlying cumulate, indicating an intrusive origin for the harrisite. Quantitative textural and chemical analysis suggests that the Cr-spinel seams formed via *in situ* crystallisation within the crystal mush together with the intrusive peridotites from an assimilation reaction between the replenishing magma and peridotitic crystal mush. Intrusive magma replenishment in Unit 10 caused significant compositional disequilibrium between the crystallising

phases in response to the postcumulus migration of reactive liquid, resulting in chemical zoning of intercumulus plagioclase crystals. We propose that the Unit 10 peridotite is intrusive and that repeated small volume magma replenishments are responsible for incremental construction of a large proportion of the peridotite body, similar to recent interpretations of parts of Unit 12 and Unit 14. Moreover, it is suggested that some or all of the injections of magma occurred into the crystal mush, rather than at the magma chamber floor. This new model of intra-mush Cr-spinel formation may have significant economic implications for PGE enrichment in other layered intrusions, such as the peridotite-hosted chromitites of the Stillwater Complex Ultramafic Series (Montana, USA). It is also worth noting that thin platiniferous chromitite seams considered to have formed *in situ* occur below the Merensky Reef of the Bushveld Complex (South Africa).

Keywords: Cr-spinel; layered intrusion; harrisite; intrusive replenishment; *in situ* crystallisation; platinum-group element

INTRODUCTION

Layered mafic-ultramafic intrusions offer excellent opportunities to study magma solidification processes in sub-volcanic systems, including the accumulation of the crystal mush and late-stage postcumulus processes (e.g., Wager & Deer, 1939; Sparks *et al*., 1985; Holness, 2007a; O'Driscoll *et al*., 2007a; Namur & Charlier, 2014; Latypov *et al*., 2015). Aside from their relevance to improving our understanding of magma differentiation and phase petrology, a handful of layered intrusions are associated with economically important base and precious metal mineralisation. Enhancing our understanding of the magma chamber processes responsible for the formation of various types of cumulate rocks thus has the potential to improve our knowledge of important ore-forming systems. The comparatively small size and young age of the Rum Eastern Layered Intrusion (ELI) provides an opportunity to see past some of the effects of postcumulus textural and mineral chemical equilibration that are common in some larger and older layered mafic-ultramafic intrusions, and study the discrete effects of magma chamber dynamics and magma replenishment in open-system layered intrusions, as well as investigate the mineralisation associated with magma replenishment.

In this study we focus on the Unit 10 peridotite portion of the ELI of the Rum Layered Suite (RLS), NW Scotland, and present new field and petrographic observations on this body of cumulate, including the important observation that numerous Cr-spinel seams exist throughout a significant proportion of its thickness. Previously reported Cr-spinel seams on Rum are mostly restricted to the boundaries between feldspathic and peridotitic cumulate (Henderson & Suddaby, 1971; O'Driscoll *et al*., 2010). Although models for the formation of stratiform Cr-spinel seams in layered intrusions are debated in the literature, they mostly call on the intrusion of new magma into the chamber (e.g., Campbell & Murck, 1993; Cawthorn *et* al., 2005; Mondel & Mathez, 2007; O'Driscoll *et al*., 2010). This leads us to consider that the Unit 10 peridotite may be formed from multiple replenishment events. Another common feature amongst many of the models for Cr-spinel seam formation is that seams are typically supposed to form at the magma-crystal mush interface (e.g., Irvine, 1977; Spandler *et al*., 2005; Mondel & Mathez, 2007; O'Driscoll *et al*., 2010; Junge *et al*., 2013). However, so-called 'subsidiary' Cr-spinel seams occur several centimetres beneath several of the ELI unit boundaries (O'Driscoll *et al*., 2009a) suggesting that some of these may form within the crystal mush. In addition, sill-like protrusions beneath the platiniferous Merensky Reef in the Bushveld Complex that are rimmed with Cr-spinel also suggest a process operating within the crystal mush (Ballhaus, 1988; Latypov *et al*. 2015), and also indicate that Cr-spinel seams in layered intrusions can form *in situ* (O'Driscoll *et al*., 2010; Latypov *et al*. 2015).

This contribution presents detailed field observations and petrography, as well as quantitative textural and mineral chemical data for rocks of the Unit 10 peridotite. A model is proposed that argues that this body was incrementally built up of multiple, small volume replenishment events. The features of the Unit 10 peridotite also suggest emplacement of magma into the crystal mush, rather than at the magma-crystal mush interface. The peridotite hosted-Cr-spinels seams also formed *in situ* during these replenishment events. The data presented here strongly suggest that crystal settling is not a viable mechanism for cumulate formation on Rum and supports the growing body of evidence that *in situ* crystallisation may be a far more common process in layered intrusions (Bédard *et al*., 1988; O'Driscoll *et al*., 2010; Latypov *et al*., 2015). In particular, the importance of *in situ* crystallisation for

Cr-spinel seam petrogenesis and associated PGE mineralisation is emphasised in this study (*cf*. Butcher *et al*., 1999; O'Driscoll *et al*., 2009b).

THE RUM LAYERED SUITE

The RLS has long been considered to represent a classic example of an open-system magma chamber which formed at ~60 ±1.3 Ma (Hamilton *et al*., 1998) as part of the British Palaeogene Igneous Province (Emeleus & Bell, 2005; Emeleus & Troll, 2014). The RLS is the type locality of 'harrisite' (Harker, 1908), a variety of peridotite comprising coarse, branching and skeletal olivine crystals, which also includes hopper olivine morphologies (*cf*. Donaldson, 1976; O'Driscoll *et al*., 2007a). The RLS is subdivided into the Eastern Layered Intrusion (ELI), Western Layered Intrusion (WLI), and Central Intrusion (CI) (Fig. 1). The ELI typifies the open-system magmatic behaviour of the intrusion as a whole, with each new major influx of magma represented by a coupled peridotite-troctolite ± olivine gabbro macro-rhythmic unit (Brown, 1956), of which there are 16 in total (Volker & Upton, 1990). Traditional models of cumulate formation for the ELI centred on the fractionation of each batch of magma via crystal (gravity) settling of successive liquidus phases to account for the transition of peridotite to more felsic cumulate. This interpretation has since been challenged with some units considered to have formed from multiple magma batches (e.g., Units 12 and 14; Renner & Palacz, 1987; Holness & Winpenny, 2008) and the peridotitic portions of some units postulated to be intrusive bodies (Bédard *et al*., 1988; Holness *et al*., 2005; 2007b). Unit 10, Brown's (1956) type unit for batch fractionation comprises the thickest peridotite layer in the ELI. Increasing Fe-content of cumulus olivine with stratigraphic height through the peridotite was taken to support this simplistic batch fractionation interpretation (Dunham & Wadsworth, 1978), with a similar argument made by Tait (1985), but invoking two separate magma replenishments instead.

FIELD RELATIONSHIPS

The Unit 10 peridotite is well exposed between Hallival and Barkeval (Fig. 1), with less well exposed outcrops around Askival and Atlantic Corrie. Figure 2 illustrates logged sections through the Unit 10 peridotite at four locations between Hallival and Barkeval (Fig. 2; with grid references for the base of

each log provided in the high resolution figure in Electronic Appendix 1). The contact between the underlying Unit 9 feldspathic cumulates is only observed at the Barkeval locality but can be inferred at the Hallival locality (Fig. 3a). On the basis of previous studies (Tait, 1985; Palacz & Tait, 1987) the ~65 m Unit 10 peridotite can be divided into a lower peridotite (LP; ~40 m) and an upper peridotite (UP; ~25 m). The relative thicknesses of the LP and UP vary slightly between the four logged sequences. The boundary between the LP and UP is sharp, with a ubiquitous 0.2–2.5 m harrisite layer separating them (Fig. 2).

The Lower Peridotite

Granular-textured peridotite is the dominant type of peridotite in the LP, and comprises layered peridotite orthocumulates. Layer thickness is variable (i.e., 0.2–1 m); layering at the finer scale (2–3 cm) is defined by the positions of Cr-spinel seams and subtle variations in the abundance of intercumulus plagioclase or clinopyroxene. Small-scale structures are observed in the layering, e.g. at the Barkeval location (Fig. 3a) where pronounced undulations occur in fine scale layering directly above harrisite layers that have extremely irregular contacts. Layer parallel foliation defined by tabular cumulus olivine crystals in granular-textured peridotite is common throughout the LP, most obvious (and strongest) in close proximity to harrisite layers. No lineation of olivine crystals was observed. Large (~40 cm) irregularly-shaped troctolite autoliths rimmed with diffuse Cr-spinel selvedges occur in granular-textured peridotite at the Barkeval location (Figure 3a; 4a, b; ~2 m above the Unit 9-10 boundary).

Harrisite layers are abundant throughout the LP. These typically have a very high proportion of intercumulus material (~40–50 vol. %), comprising plagioclase and clinopyroxene, often with cm-sized skeletal olivine visible at outcrop (Fig. 5a; h). Textural variation of harrisite is also evident in the field, in the form of patchy layers composed of varying grain sizes of skeletal harrisitic olivine (Fig. 3a; 5b). Contrary to previous work on harrisites (e.g., Donaldson, 1974; O'Driscoll et al, 2007a) the long axes of skeletal olivine are rarely perpendicular to the top and base of the layer, and are randomly arranged. Packages of harrisite layers can be correlated from one log to the next (see Fig.

2), but the correlation of certain layers is not possible due to the bifurcation, tapering and complete lateral termination of some layers along strike (Fig. 2; 3b). Where the layers do not terminate, harrisite layers can be often be traced tens of metres across the entire length of the outcrop. The thickness of harrisite layers is highly variable (0.2–4 m) and based on field observations and the logged sections, it is tentatively suggested that some layers (and packages of layers) increase in thickness away from the postulated feeder zone for the intrusion, the Long Loch Fault (Emeleus *et al*., 1996; Fig. 2). Harrisite layers have flat-to-broadly undulose bases while their tops range from being flat-to-extremely irregular (Fig. 3c). The upper contacts of harrisite layers exhibit irregularities on their upper surfaces, with more pronounced examples of such apophyses evident around Barkeval (Fig. 3c; 5c). Less extreme irregularities in the upper and lower contacts of peridotite layers occur with distance away from the Long Loch Fault (Fig 5d). Harrisite layers taper and terminate against granular peridotite, still with irregular upper surfaces (Fig. 5e; h). Variably sized (10–30 cm) granular-textured peridotite autoliths are recorded in some thicker (> 1 m) harrisite layers. Olivine grain size is significantly reduced in the granular-textured peridotite autoliths (~1 mm), with a noticeable accompanying reduction in the proportion of intercumulus minerals (≤ 10 vol. %).

Cr-spinel seams are extremely abundant within the LP, occurring in both granular-textured peridotite and harrisite. The occurrence of Cr-spinel seams is typically accompanied by a relative increase in the proportion of intercumulus plagioclase within the seam. Individual seams are not laterally extensive and can rarely be traced over more than several tens of metres. Seam thickness is highly variable (2–20 mm), with an average thickness of 4–5 mm. The textures of the Cr-spinel seams are comparable to peridotite-hosted seams observed in the Unit 12 peridotite (*cf*. O'Driscoll *et al*., 2010), which were described by those authors as 'chain-textured' where the Cr-spinel occurs in intercumulus plagioclase and surrounds cumulus olivine crystals. The texture of the seams is consistent irrespective of peridotite lithology. Only one of the seams studied here is not chain-textured, and no cumulus olivine was observed within the upper and lower limits of the seam (Fig. 3c; 4c). This seam also exhibits irregularities (depressions and culminations) along strike (Fig 4c). Significant undulations, even apparent discontinuities, of Cr-spinel seams can occur above harrisite layers (Fig. 4b).

It is important to specify that many of the Cr-spinel seams referred to here are not chromitite, *sensu stricto,* i.e., they often contain << 60 vol. % Cr-spinel. They are referred to here as 'Cr-spinel seams' because the Cr-spinel is often more diffusely disseminated than in some of the other well-known Rum seams (*cf.* O'Driscoll *et al*., 2010). However, the Cr-spinel seams are still considered to represent clearly delineated 'events' (horizons) within the cumulate pile.

The Cr-spinel seams can be broadly divided into four groups based on their lithological relationships to surrounding peridotite: granular-textured peridotite-hosted seams, boundary seams, harrisite-hosted seams, and foliated peridotite-hosted seams. Granular-textured peridotite-hosted seams occur with no obvious textural or mineralogical variation above or below the seam (Fig. 4e). Boundary seams occur with obvious textural (or mineralogical) variation in the peridotite above and below the seam, such as Cr-spinel seams that occur between harrisitic and granular-textured peridotite (Fig. 4f). Harrisite-hosted seams occur within individual harrisite layers. These seams are the most discontinuous and are also not layer-parallel, but have an undulose character. While harrisite hosted seams are often not layer-parallel, no vertically-oriented Cr-spinel seams were found in the Unit 10 peridotite. Foliated peridotite-hosted seams occur locally where the cumulus olivine is tabular or elongated (including harrisitic olivine), and defines a foliation within the upper and lower confines of the Cr-spinel seam. The character (i.e., type) of Cr-spinel seam can also change along the lateral extent of a given seam, particularly where harrisite layers terminate, but their associated seams continue laterally (Fig. 5f).

The Upper Peridotite

The UP is best exposed in the two Hallival logged sections (Fig. 2), where there is near continuous outcrop into the overlying feldspathic cumulates. The UP is relatively homogenous, comprising a texturally distinctive clinopyroxene-oikocrystic peridotite (Fig. 4g). However, the lowest ~3 m of the UP is distinctly less pyroxene rich (Fig. 3e). The UP is predominantly massive, with layering locally defined by harrisite layers toward the top (Fig. 2; 3e, f). These harrisite layers contain clinopyroxene oikocrysts like the surrounding granular-textured peridotite. Other harrisite layers in the UP have 'hopper-textured' olivine crystals (see Donaldson 1976), and share similar morphological

characteristics to harrisite layers within the LP, with flat bases and variably irregular top surfaces. Harrisite layers in the UP can occur as discordant (sub-vertical) sheets (Fig. 4h), as well as layer-parallel sheets. Cr-spinel seams are absent from the UP. Gabbroic pegmatite veins are common throughout the UP, composed of ≤ 2 cm euhedral clinopyroxene and subhedral plagioclase crystals, with rarer ~5 mm equant olivine crystals. These pegmatites become extremely common towards the top of the UP, where they occur as ≤ 10 cm thick vertical sheets. The boundary between the UP and overlying feldspathic cumulates is marked by a ~20 cm thick gabbroic pegmatite layer (Fig. 3e).

PETROGRAPHY

The Lower Peridotite

The cumulus mineralogy of the granular-textured peridotite is dominated by rounded, euhedral (~0.5–3 mm) olivine crystals. Small numbers of crystals with tabular (elongate) and hopper crystal morphologies (~3–5 mm) occur in most samples; with increased abundances of the latter in coarser-grained granular-textured peridotites. Olivine crystals close to Cr-spinel seams often show a reduction in grain size and abundance of apparent triple junctions with 120° dihedral angles (e.g., Figure 6d). Euhedral Cr-spinel crystals (~0.3 mm) occur outside of Cr-spinel seams in accessory proportions (~1 vol. %). Noticeably finer-grained (~0.1 mm) Cr-spinel inclusions occur within some olivine crystals, but these are comparatively rare. The volume proportion of intercumulus material varies between 10–25%. The intercumulus mineralogy is dominated (≥ 85%) by plagioclase oikocrysts (0.5–5 mm), with subordinate diopside oikocrysts. Zoning of the intercumulus plagioclase is visible under the petrographic microscope, including rare oscillatory zoning (Fig. 6a; 6b, see also Fig. 15). As noted above, foliation is common, defined by elongate or tabular olivine crystals (Fig. 6c). Apatite, biotite, serpentine, chlorite, calcite, epidote and kaersutite/titano-pargasite occur as accessory phases, typically in the interstices of the olivine framework.

Harrisite in the LP consists of approximately equal-to-subequal proportions of cumulus and intercumulus minerals. Olivine crystal morphologies in harrisite are dominated by very coarse-grained hopper and highly skeletal olivine crystals. The most elongate crystals can be up to several

centimetres long. The intercumulus mineralogy comprises very coarse-grained (≤ 3 cm diameter) plagioclase and diopside oikocrysts, with average overall proportions of 70:30, respectively. Trace amounts of serpentine, chlorite, calcite, epidote, biotite and amphibole also occur.

Cr-spinel seams in the Unit 10 peridotite are chain-textured (with the exception of one sample; Fig. 3, 6d). The constituent Cr-spinel crystals occur in the intercumulus minerals between and around cumulus olivine crystals (Fig. 6e). The Cr-spinel crystals are euhedral and have a consistent grain size range of 0.05–0.3 mm, with an average crystal size of ~0.2 mm. The average crystal size in harrisite tends to be ~0.3 mm. Polygonal Cr-spinel crystal aggregates are locally observed, resulting in subhedral-euhedral crystal shapes and a corresponding grain size increase that can be detected via reflected light microscopy. Cr-spinel is enclosed by intercumulus plagioclase oikocrysts, and more rarely by intercumulus clinopyroxene. A common textural feature is the occurrence of Cr-spinel adjacent to embayments in cumulus olivine crystals (Fig. 6e). Ilmenite exsolution lamellae occur in Cr-spinel, but typically in crystals that do not occur in seams. Base-metal (Ni-Cu) sulphides also occur very closely associated with Cr-spinel (Fig. 6f), often moulded onto or touching Cr-spinel grains. Where sulphide grains occur, magnetite is also present, seemingly attached to the Cr-spinel crystals (Fig. 6g). Platinum-group minerals (PGM) including Pt-arsenides/tellurides, Pd-antimonides, Ru-Ir alloys and Pt-Ir sulphosalts, as well as electrum (Au-Ag) grains, occur closely associated with these sulphides (Fig. 7; 8).

The Upper Peridotite

Cumulus olivine crystals in the UP have a heterogeneous texture, consisting of granular-textured (equant) olivine as well as elongate/tabular olivine (~2 mm long) with subordinate, coarser-grained (~4 mm) hopper and skeletal olivine (see Fig. 6h). Cr-spinel occurs between cumulus olivine, enclosed by intercumulus clinopyroxene and plagioclase. Disseminated Cr-spinel is more abundant in the UP than in the LP (i.e., up to 5 vol. %). The proportion of intercumulus minerals accounts for 15–25 vol. % of the rock, and these comprise plagioclase oikocrysts (1–2 mm diameter) and larger (5–20 mm) rounded-elongate oikocrysts of diopside. The volume percentage proportion of intercumulus

plagioclase to diopside is 60:40, respectively. Compositional zonation is also optically apparent in intercumulus plagioclase, as observed in the LP. A non-pervasive foliation of variable strength, carried by the tabular olivine crystals, is common throughout the UP, oriented approximately parallel to layering.

CRYSTAL SIZE DISTRIBUTION ANALYSIS

Method

Crystal Size Distribution (CSD) analysis provides a quantitative means of measuring the grain size and number of crystals within a defined area of a sample of interest. As crystal size carries important information on cooling and nucleation rates within igneous rocks, CSDs have been used to infer crystallisation kinetics in magmatic systems independent of experimental or thermodynamic approaches (e.g., Cashman & Marsh, 1988; Marsh, 1998; Boorman *et al*., 2004). It has been argued that simple crystallisation within either an open-system (steady-state) or closed-system (batch) end-member environment produces straight (or log-linear) CSD profiles that simply represent the nucleation and growth of crystals as magma cools and solidifies (Marsh, 1998). Deviation from this log-linear shape (e.g. CSD kinking or curvature) has been attributed to various processes such as crystal accumulation and removal (Marsh, 1998), multiple crystal populations (Higgins, 1994; Marsh, 1998), postcumulus crystal coarsening by annealing and Ostwald ripening, or compaction (Boorman *et al*., 2004; Higgins, 2002b). Log-linear CSDs can be further analysed by plotting derivative CSD parameters against one another (e.g., characteristic length versus intercept). Such parameters have been shown to have a relationship irrespective of the modal abundance of the mineral of interest (Higgins, 2002a).

In this study, CSDs are employed to support the petrographic observations in determining the environment of crystallisation of Cr-spinel seams and to aid in ascertaining the relative importance of magmatic and postcumulus processes during their formation. The CSDs were determined from thin sections and calculated following the methods outlined in Higgins (2000; using the program *CSDCorrections version 1.4*). The CSDs were calculated by manually digitising reflected light photomicrographs, recommended for opaque phases to avoid misidentification of annealed Cr-spinels

(O'Driscoll *et al*., 2010; Vukmanovic *et al*., 2013). The digitised images were analysed using *ImageJ* image analysis software to determine the input parameters for *CSDCorrections*. Feret length, the length of a square with an area equal to that of the analysed crystal, has been employed as a crystal size parameter here, following the method of O'Driscoll *et al*. (2010). No preferred orientation of Cr-spinel crystals was observed. An aspect ratio of 1:1:1 and a roundness factor of 0.5 were input into *CSDCorrections*. In total, CSDs were produced for Cr-spinel seams from 16 samples, incorporating the different seam groups introduced above, as well as accounting for differences within the seam groups defined above (such as seam thickness). A minimum of 500 crystals was analysed in each sample where possible to obtain a statistically viable representation of each seam (Mock & Jerram, 2005). As the smallest crystals are easily visible in reflected light, the lower crystal size limit of 0.01 mm is taken to represent the true lower limit of the sample.

Results

Crystal Size Distribution plots are illustrated in Figure 9, with additional CSD output data in Electronic Appendix 2. Previously published CSD data for the Unit 11-12 main Cr-spinel seam and so-called peridotite-hosted 'supra-seams' above the Unit 11-12 boundary (O'Driscoll *et al*., 2010) are included for comparison in Figure 9. All CSD plots display log-linear profiles at larger size fractions with perturbations in some of the profiles occurring for smaller size fractions. There is modest variation within the specific groupings of seams distinguished above (Fig. 9). For example, CSDs for granular-textured peridotite-hosted seams define a range of slope values from -55.0 to -21.2 mm^{-1}. The profiles are broadly log-linear, with shallowing of the CSD slope typical at smaller size fractions. Boundary seams show very similar profiles to those of the granular-textured peridotites, with slopes that range from -48.4 to -27.1 mm^{-1}, log-linear profiles, and a shallowing of slopes at the smallest size fractions. The harrisite-hosted seams have CSDs with similar slopes to the aforementioned groups (-55.1 to -19.5 mm^{-1}), with the shallowest slopes measured in this study. They also exhibit further shallowing at smaller size fractions. Seams hosted within foliated peridotites display similar slope values to those in previous groups, for the largest size fraction, but are characterised by broad overturns at the middle-to-smallest crystal size bins. Kinking of the CSD profiles is observed for some

granular-textured and boundary group seams. These size bins are typically associated with large uncertainties, and as such caution must be taken when interpreting the CSD profile.

A plot of characteristic length (-1/slope; see Higgins, 2002a) versus intercept (Fig. 10a) distinguishes the Cr-spinel seams groups, i.e., granular, boundary, harrisite-hosted, previously recognised on field evidence, with groupings of the granular, boundary, and harrisite hosted seam groups. The foliated seam group does not produce a distinctive group. Instead, these data plot within the granular grouping irrespective of the peridotite host (i.e., harrisitic or granular). The volume percentage of Cr-spinel from both *ImageJ* and *CSDCorrections* show a strong correlation (Fig. 10b). A good correlation also exists between the measured volume phase proportion and the *CSDCorrections* regression (calculated in *CSDCorrections 1.4*; see Higgins, 2002a), supporting a true log-linear profile (Fig. 10c). Deviation from this 1:1 fit occurs in samples that have the strongest perturbations from a log-linear profile, such as foliated and harrisite-hosted samples where the changes in CSD slope occur at small size fractions. The CSD data fall below the closure limits defined by assuming 100 vol. %, of the mineral phase of interest (Higgins, 2002a; Fig. 10d) which is a useful indicator of the robustness of the CSD dataset.

WHOLE ROCK GEOCHEMISTRY

Methods

Major element analysis was performed by X-ray Fluorescence (XRF) at Bureau Veritas Minerals, in Vancouver, Canada. Centimetre-sized slabs of rock were prepared to remove altered and weathered surfaces before being cleaned with de-ionised water and dried at 50°c for several hours. Samples were then crushed to < 75 µm and fused with $Li_2B_4O_7/LiBO_2$ before being analysed by XRF. Repeat analysis of one sample was performed with reproducibility < 1%. Details on the detection limits and standards used in analysis can be found in Electronic Appendix 3.

Results

The major element geochemistry for samples in this study are summarised in Table 1 and Electronic Appendix 3. The samples display modest variation in their major element composition and can be

broadly delineated into groups corresponding to lithology (Fig. 11). Harrisites have the lowest MgO and FeO_t contents (28.71–32.87, and 11.01–12.28 wt. %, respectively) and the highest Al_2O_3 abundance (7.41–8.43 wt. %). The harrisites are compositionally more similar to Sample M9, a porphyritic picritic dyke (Upton *et al*. 2002), than the granular-textured peridotites. Granular-textured peridotites have a range in MgO and FeOt of 34.91–35.53, and 13.08–13.32 wt. %, respectively, with sample Gra-2B, as a coarse granular–harrisitic peridotite with intermediary MgO values (32.91 wt. %) between both groups. Cr_2O_3 wt. % between the sample groups is largely dependent on lithology (specifically Cr-spinel content), with similar Cr_2O_3 values between peridotite types (Fig. 11). The UP sample is broadly similar to the lower peridotite, but contains elevated FeOt (14.37 wt. %), which is comparable to values presented by Tait (1985).

MINERAL CHEMISTRY

Methods

Mineral chemical data were obtained using a JEOL JXA-8900RL electron microprobe at the Department of Geochemistry, Geowissenschaftliches Zentrum der Universität Göttingen (GZG) in 2014. The Cr-spinel compositions were obtained using an acceleration voltage of 20 kV with a beam current of ~20 nA and a typical beam diameter of ~1 μm. Cr-spinel count times on peak and background for Mg, Al, Cr, Fe and Si were 15s and 5s, respectively, and for V, Ti, Mn, Ni, Zn were 30s and 15s, respectively. Olivine compositions were obtained using an acceleration voltage of 15 kV, with a beam current of ~15 nA and a typical beam diameter of ~5 μm. Olivine count times on peak and background for Si, Mg, Al were 15 s and 5 s, respectively, for Fe, Mn, Ni were 30 s and 15 s, and 60 s and 30 s for Ca. Element maps of Na concentration were carried out on three samples where optical zonation of intercumulus plagioclase was observed under the petrographic microscope within the LP. One Cr map was also collected on a sample of a large clinopyroxene oikocryst from the UP. Sample locations can be found in Electronic Appendix 1. Element maps were obtained using an acceleration voltage of 20 kV, with a beam current of ~60 nA, a beam diameter of 2 μm and a dwell time of 50 ms.

Cr-spinel compositions were measured from 11 Cr-spinel seams; the measurements were made along three vertical traverses for each seam, with an average of 15 Cr-spinel crystals analysed per traverse. The traverses were approximately equidistant from one another (5–7 mm) along strike. Each traverse typically included several peridotite-hosted Cr-spinel crystals for comparison, above and below the seam. All of the Cr-spinel crystals analysed were hosted in plagioclase oikocrysts. Disseminated Cr-spinel were analysed in the UP, which lacks discrete seams. The ferric iron content of Cr-spinel was calculated following Droop (1987), which assumes that the spinel composition is stoichiometric. As such, Cr-spinel compositions rich in a ferric iron component should be treated with caution (*cf.* Quintiliani *et al.*, 2006; O'Driscoll *et al.* 2010).

Results

Olivine

The olivine chemical data discussed here are tabulated in Electronic Appendix 4. Olivine compositions in the Unit 10 peridotite have high-Fo values, with a narrow range between Fo 82–88 mol. %. Nickel concentrations range between 1832–3029 ppm (Fig. 12). There are no discernible differences in olivine compositions from the different LP peridotite types (granular-textured, harrisitic etc; Fig. 12). However, olivine from the UP has a generally lower Fo content than the LP olivines (Fo 82–84), with similar Ni concentrations of 1951–2556 ppm.

Cr-spinel

The full Cr-spinel chemical dataset discussed below is presented in Electronic Appendix 5. Cr-spinel chemistry is highly variable between samples but no well-defined groups can be delineated. Previously published data for peridotite-hosted Cr-spinel from the RLS has been included for comparison (Upton *et al.*, 2002; O'Driscoll *et al.*, 2009a; Holness *et al.*, 2007; Fig. 13a). Chromium number (Cr#; $[Cr^{3+}/(Cr^{3+}+Al^{3+})]$) values are similar for Cr-spinel between peridotite types, but vary within and outside the seams. Magnesium number (Mg#; $[Mg^{2+}/(Mg^{2+}+Fe^{2+})]$) values for Cr-spinel within the seams varies between 16 and 59. There is no distinct chemical variation between the granular, boundary and foliated seam groups (Fig. 13b). However, harrisite-hosted Cr-spinel crystals

are generally characterised by higher Cr# values (corresponding to lower Al_2O_3), and higher Fe_2O_3 (~17 wt. %) values, compared with ~14 wt. % Fe_2O_3 for granular, boundary and foliated seam types. Cr-spinel compositions in peridotite above and below the seams are also typically higher in Fe_2O_3 (Fig. 13b) and TiO_2- the latter varies from 0.71 to 5.80 wt. %. Cr-spinel compositions analysed from the UP differ significantly from those in the LP. Specifically, Cr_2O_3 content in the UP is considerably lower (25–32 wt. %), Fe_2O_3 content is higher ~23 wt. %, and TiO_2 contents are typically > 3 wt. %.

Cr-spinel from seams in Unit 10 exhibit compositional variation across individual traverses at the mm-scale. Similar patterns are observed from one seam to the next (Fig. 14). For example, Cr# is lower within seams, compared to higher Cr# values of Cr-spinel above and below the seams. This reflects an increase in Al_2O_3 within seams, with a concomitant increase in Fe_2O_3 away from the seam (see also Fig. 13b). TiO_2 is particularly low within seams, but increases significantly (up to 5.8 wt. %) with distance away from the seam and into the surrounding peridotite. This is shown particularly well in Sample U10M (Fig. 14). This sample contains a relatively thick seam and a secondary diffuse seam several millimetres above the former. The TiO_2 values increase away from the thick seam, but decrease again as the diffuse seam is approached. Additional detail on Cr-spinel chemical variation across these traverses can be found in Electronic Appendix 5.

Element Maps

Na maps of optically-zoned intercumulus plagioclase from the Cr-spinel seams show both normal and reverse compositional zoning (Fig 15), as well as an example of well-developed oscillatory zoning (Fig. 15a). Sample U10A, from a granular-textured seam displays well-developed oscillatory zoning (Fig. 15a). Sample U10R, from a foliated-type seam, exhibits patchy reverse zoning of the intercumulus plagioclase (Fig. 15b). Sample U10B displays normal zoning located < 5 mm above a boundary seam that occurs on the top of a harrisite layer (Fig. 15c). Here, the cores of some of the intercumulus plagioclase crystals are markedly rectilinear, with seemingly rounded or subhedral rims. Zonation of intercumulus plagioclase is also apparent in the QEMSCAN® images (Fig. 7). While quantitative analyses of the mapped plagioclase crystals are not available, published and unpublished mineral chemical data for zoned cumulus and intercumulus plagioclase crystals from the Rum ELI

indicate that variation of ~An_{83}–$An_{74,}$ and ~An_{74}–An_{63} occurs (O'Driscoll *et al*., 2009a; Hepworth, unpublished data). Element mapping on a clinopyroxene oikocryst from the UP reveals patchy zoning of Cr (Fig. 15d), similar to that reported in Unit 9 (Leuthold *et al*., 2014).

DISCUSSION

Intrusive Replenishment in the Rum Layered Suite

Harker (1908) originally considered the peridotite portions of the ELI rhythmic units to be intrusive. However, subsequent work on the ELI by Brown (1956) that was almost certainly influenced by studies of the Skaergaard Intrusion (Greenland), invoked fractional crystallisation and gravity (crystal) settling instead (Wager & Deer, 1939). Bédard *et al*. (1988) first challenged this model and instead suggested, like Harker (1908), that the peridotites of the ELI intruded into a pre-existing troctolitic crystal mush. Bédard *et al*. (1988) suggested that it was possible that all of the peridotite bodies of the ELI could be intrusive. More recently, detailed textural and geochemical studies of the Unit 9 peridotite, in particular, have demonstrated the intrusive nature of this body and shown that it modified (texturally and chemically) the feldspathic cumulate above and below it (Holness *et al*., 2007b; Leuthold *et al*., 2014). Whilst the importance of open-system magma chamber systematics has been emphasised for the RLS in general (Renner & Palacz, 1987; O'Driscoll *et al*., 2007a; 2007b; Holness & Winpenny, 2008), further evidence of intrusive peridotites has not specifically been mentioned in the ELI. Here, we argue that the Unit 10 peridotite is composed of multiple small volume intrusive replenishment events.

Intrusive harrisite

The Rum harrisites are a type example of crescumulate, as defined by Wager *et al*. (1960). The authors envisaged dendritic and skeletal olivine crystals growing upward from the contemporary magma chamber floor. As such, these rocks have become an important example of *in situ* crystallisation in layered intrusions. While the model of Wager *et al*. (1960) accounts for those olivine crystals that demonstrably grew upwards from a substrate, Donaldson (1974; 1975) highlighted the problems of the model in explaining apparently downward growing harrisitic olivine, or crystals with

stellate morphologies that also frequently occur in these layers. Experimental studies that reproduced harrisitic olivine textures indicate that these rocks probably form relatively rapidly, under enhanced undercooling of picritic magma (Donaldson, 1975; Lofgren & Donaldson, 1975; O'Driscoll *et al*., 2007a). Upton *et al*. (2002) further highlighted the important role picrite played as a parental magma to the RLS. O'Driscoll *et al*. (2007a) suggested that the enhanced undercooling that gave rise to harrisitic texture occurred in thin sheets of newly emplaced picrite at the base of the magma chamber. One implication of this idea is that the WLI (Fig. 1), where most of the Rum harrisite occurs, was built up of numerous small volume replenishments.

Multiple features of the Unit 10 harrisite layers are not consistent with processes that occurred at the magma-crystal mush interface (e.g., Fig. 2; 5c). Irregular upper surfaces, tapering and termination of harrisite layers have been reported from harrisites in the WLI, where they were considered to represent ponded intercumulus liquid from layers above or below the harrisite in question (Donaldson, 1982). This is significant, as it suggests that harrisite might form within the crystal mush. However, the lateral correlation of packages of harrisitic layers across hundreds of metres of Unit 10 stratigraphy (as suggested in Fig. 2) is not consistent with ponding of intercumulus liquid, especially as these layers also change in thickness, and may even cut across surrounding layers (Fig. 2). In our view, the tapering, bifurcation and complete termination of some harrisite layers and pose problems for a model invoking ponding of intercumulus melt or magma chamber floor processes. Instead, we suggest that these layers represent sill-like intrusions of picritic magma emplaced directly into the crystal mush as semi-stratiform intrusive bodies, similar to interpretations made by Bédard et al. (1988) in the ELI, and also to sill-like injections of komatiites observed in lava piles by Houlé *et al*. (2009). It is also suggested that large amplitude (> 50 cm) irregularities (Fig. 5c; d) on the upper surfaces of harrisite layers are best considered as features associated with intrusive sheets. It is not considered likely that structures such as that illustrated in Figure 5c could have been preserved on the magma chamber floor without collapsing. Instead, loading of a newly intruded and rapidly crystallising picritic sheet by the overlying crystal mush might explain such apophyses (Fig. 5c; d; see discussion below). There is a suggestion in Figure 2 that harrisite layers (and packages of layers) thicken with distance away from the feeder zone (Long Loch Fault), an observation that might be

explained by considering the competency of the crystal mush. Further from the feeder zone, the crystal mush may have been cooler and more rheologically competent, such that thicker harrisite layers (associated with greater degrees of undercooling) could intrude. Finally, the granular-textured peridotite on either side of some harrisite layers exhibits extreme reductions in porosity (i.e., intercumulus mineral fraction) and well-developed textural equilibration. In the latter, the 2D apparent triple junctions of polygonal olivine grains approach 120° (see Fig. 6d), suggesting a degree of thermal maturation (*cf.* Holness, 2007a), which might indicate a contact metamorphic effect on either side of the intrusive harrisite sheets. To what extent the host (granular-textured) peridotite was solidified in each instance of harrisite emplacement (i.e., exactly how much intercumulus melt remained in the host) is difficult to estimate, but may have been variable for different layers.

An important premise of harrisite formation is that the replenishing magma is aphyric (Donaldson, 1974; 1975; O'Driscoll *et al*., 2007a). Higher degrees of undercooling with homogenous nucleation of olivine led to the extremely large (> 1 m long) dendritic olivine crystals that are observed in the WLI. The degree of undercooling (and supersaturation in olivine) has been experimentally shown to have a control on olivine morphology (Donaldson, 1974; 1976; Faure *et al*., 2003; Welsch *et al*., 2014), suggesting that the different harrisite layers of the WLI formed from different degrees of undercooling. This is not surprising, given that the multiple replenishments that fed the Rum intrusion are likely to have varied in volume (*cf.* O'Driscoll *et al*., 2007a). In the case of the Unit 10 peridotite, however, the lack of extremely coarse-grained dendritic crystals and the relative abundance of hopper olivine crystal morphologies suggest that the degrees of undercooling may have been comparatively lower than in parts of the WLI. The whole rock chemistry suggests harrisites are slightly more compositionally evolved than the granular-textured peridotites, with lower MgO (Fig. 10). However, lower FeO_t contents than granular-textured peridotites point towards a more primitive composition, while Cr_2O_3 contents remain broadly similar between peridotite types. The mineral chemistry of olivine and plagioclase strongly suggest they crystallised from the same magma, with no variation in olivine compositions between different rock types (Fig. 12). The strong modal variation in mineralogy (i.e., harrisite contains a greater modal abundance of feldspar) explains this variation in whole rock chemistry and supports the argument for the two peridotite types crystallising

from the same magma, but under different conditions. There are several possible reasons for the difference in crystallisation conditions. One might be that the parental melt batches that formed the Unit 10 peridotite may not have arrived at the level of the magma chamber in a completely aphyric state. Donaldson (1976) suggested that the presence of pre-existing nuclei may decrease the growth rate of spontaneously nucleating nuclei, ultimately suppressing the degree of supersaturation and forming less skeletal olivine morphologies. This might imply that peridotites forming the Unit 10 peridotite formed from a mixture of relatively aphyric and phyric magmas, now represented by harrisitic and granular-textured peridotite, respectively. With respect to the WLI, it might be expected that the ELI did not form from magmas that were as primitive (or superheated with respect to olivine). By the time the structurally higher ELI formed, the RLS was a well-established (thermally mature) system, compared to the WLI which lies towards the base of the intrusion and whose parental melts might have encountered a much steeper thermal gradient on entry to the magma chamber. O'Driscoll *et al*. (2007a; 2010) argued that the melts that formed the WLI were likely to have been aphyric, and also that features at some ELI unit boundaries (e.g., Unit 7-8) suggested emplacement of high-temperature aphyric picrites. By contrast, the textural study of Worrell (2002) found evidence of multiple crystal populations in the WLI and suggested that the granular-textured peridotites there formed from phenocryst-rich magmas. The model of O'Driscoll *et* al. (2007a) for harrisite formation might also be adapted for the Unit 10 peridotite, where the intruding picrite instead comes into contact with relatively cold cumulate or crystal mush, enhancing undercooling. This is supported by the presence of brittle deformation of layers above harrisite apophyses and the lack of cross-cutting of these apophyses by other peridotites types.

The physical state of the host crystal mush is an important factor in explaining the relationships at the boundaries between harrisites and granular-textured peridotites. In particular, it is possible that some of the complexity at harrisite upper surfaces arises as a result of the rheological contrast between the 'orthocumulate' harrisite and the more mesocumulate-like granular-textured peridotite. Because of its greater volume of interstitial melt (as represented by intercumulus plagioclase), harrisite might remain 'mushy' longer than the peridotites above and below. Indeed the greater volume of plagioclase in harrisite might therefore be expected to have lower solidus temperatures.

The movement of interstitial melt from the intruded harrisite layers following emplacement could explain the irregularities and apophyses observed, as well as the associated deformation of layering that occurs adjacent to harrisite layers (e.g., Fig. 5c). However, this would be expected to result in distinctly olivine-poor apophyses, which are not present. In fact, harrisitic textures in the apophyses are similar to those in the main layered from which they are assumed to have originated. From this, we suggest that the apophyses represent primary melt intrusion features at the boundaries of the conduits that facilitated harrisite emplacement, perhaps forming at points where the host cumulate was less well solidified or where brittle deformation opened up fractures in the wall rock.

We therefore argue that most, if not all, of the harrisite sheets in the Unit 10 peridotite are intrusive. There is evidence that the granular-textured peridotite may also be intrusive, i.e., where Cr-spinel seams bound layers of such rock. We conclude that the physical properties of the resident crystal mush, the phenocryst content of the intrusive magma, or a combination of both played a critical role in the development of the different peridotite types in Unit 10.

In situ Cr-spinel seam formation within a crystal mush

The processes by which stratiform Cr-spinel seams form in layered intrusions is contentious, and a wide range of models have been proposed to explain their occurrence, including pressure changes, magma mixing, cumulate and wall-rock assimilation, emplacement as crystal cargos, accumulation by crystal settling and formation from a stratified magma column (Henderson & Suddaby, 1971; Irvine, 1977; Lipin, 1993; Spandler *et al*., 2005; Mondal & Mathez, 2007; O'Driscoll *et al*., 2009a; 2010; Junge *et al*., 2014). Many of the above models rest on the observation that Cr-spinel seams occur at levels of the intrusion stratigraphy associated with the introduction of new magma (i.e., replenishment, in an open-system magma chamber). The Unit 10 peridotite contains dozens of Cr-spinel seams, and we consider the most likely explanation for this is that the peridotite body represents multiple replenishment events. Many of the published models for Cr-spinel seam formation assume that the horizon is formed at the magma-mush interface on the magma chamber floor, with a few exceptions (e.g., Voordouw *et al*., 2009). This presents a problem when considering the close spatial relationship of the Unit 10 Cr-spinel seams with intrusive harrisite and other peridotite layers.

However, the possibility that Cr-spinel seams can form within the crystal mush has previously been suggested for the Bushveld Complex by Ballhaus (1988) and later by Latypov *et al*. (2015), where sill-like harzburgite protrusions that are rimmed with Cr-spinel occur beneath the platiniferous Merensky Reef. In addition, the felsic cumulates beneath the Unit 7-8 and 11-12 boundaries in the Rum ELI contain 'subsidiary' seams, which have been attributed to formation within the crystal mush by O'Driscoll *et al*. (2009a; 2010). We propose here that the Unit 10 peridotite seams form *in situ*, a notion that has previously been suggested for other chromitite seams within the RLS (O'Driscoll *et al*., 2009a; 2010, Latypov *et al*., 2013), and other intrusions (e.g., Barnes & Jones, 2013).

Previously reported observations that the Cr-spinel seams in the ELI follow culminations and depressions (and even overhangs), without changing thickness, show that crystal settling is not a likely mechanism for accumulation of the Cr-spinel (O'Driscoll *et al*., 2010; Latypov *et al*., 2013). In this study, it is shown that Cr-spinel seams can have a close relationship with the interior, upper, and basal surfaces of intrusive harrisite sheets. The CSD data presented here for the Cr-spinel seams provide further support for crystallisation *in situ* (Fig. 9). Most of the Unit 10 Cr-spinel seams CSDs have a log-linear profile for most crystal sizes, suggesting a relatively simple relationship between nucleation and growth. The lack of a dominance of larger crystal sizes, or evidence of size-dependent mechanical sorting (Marsh, 1998; Higgins, 2002b), argues against crystal settling. Similar CSD profiles are observed from other Cr-spinel seams in the ELI (O'Driscoll *et al*., 2009a; 2010), and the Coobina Layered Intrusion in Western Australia (Barnes & Jones, 2013) where *in situ* crystallisation has also been invoked. However, the smallest and largest crystal size bins of some of the CSDs show additional complexity. Shallow slopes and downturns at the smallest crystal size fraction likely reflect postcumulus coarsening or annealing (i.e., Ostwald ripening). The CSD profiles for boundary seams and granular-textured peridotite-hosted seams have relatively similar slopes. However, harrisite-hosted Cr-spinel seams typically display shallower profiles and are dominated by larger crystal sizes overall. This is attributed to interaction with the large interstitial melt component that the harrisitic mush contained, evidenced by the large proportion of intercumulus material. Conversely, in boundary seams and granular-textured peridotite-hosted seams the intercumulus component is much lower, suggesting a greatly reduced potential for interaction and postcumulus modification of Cr-spinel with

intercumulus melts. The CSD data suggest that the Cr-spinels from the foliated peridotites may have also undergone a form of Ostwald ripening. It is possible that the formation of the foliation affected the Cr-spinel texture, perhaps by loss of smaller nuclei and crystals during compaction-related expulsion of intercumulus melt (Higgins, 2002b).

The chemistry of the Cr-spinel across seam types (and textures) is generally consistent, suggesting similar processes operating during petrogenesis. The exception to this may be harrisite hosted Cr-spinels which display slightly more Fe_2O_3 rich compositions, consistent with their interaction with intercumulus liquid in the porous harrisitic crystal mush (e.g., O'Driscoll *et al*. 2009a; Leuthold *et al*. 2014). Compared to previously reported peridotite hosted Cr-spinel compositions in the ELI, the Unit 10 Cr-spinel spans much of the range of previous analyses. The consistency of chemical composition of Cr-spinel within peridotites alludes to a potentially significant control of host lithology/mineralogy on Cr-spinel composition, whereas in feldspathic hosts Cr-spinel can show either extreme Al-enrichment (O'Driscoll *et al*., 2010) or Fe-enrichment (Henderson, 1975; O'Driscoll *et al*., 2009a; Lenaz *et al*., 2013; Leuthold *et al*., 2014).

Chemical traverses through the seams and surrounding peridotite reveal mirrored trends in Cr# and TiO_2 (Fig. 14). There is an increase in Cr# with distance, above and below the seam, implying that the Cr-spinels in the seam have the highest Al_2O_3 contents. Following Bell & Claydon (1992) and O'Driscoll *et al*., (2009a; 2010) we interpret the latter Cr-spinel compositions as the closest to those originally crystallised from magma, a suggestion further supported by recent experimental data reported by Leuthold *et al*. (2015). Away from the seam, the increase in Cr# and concomitant increase in Fe_2O_3 suggest a greater degree of interaction with intercumulus melt in the host peridotite. This is observed in all datasets where Cr-spinel occurs outside the limits of a given seam (Fig. 13b). The lack of modification within the seam possibly results from a buffering effect of the liquid after Cr-spinel crystallisation or from the effect of reducing porosity once Cr-spinel has crystallised, reducing the ability of liquids to penetrate the seam, or from a combination of both. Notably, TiO_2 also increases with distance from the seams (Fig. 14). Maximum TiO_2 contents of up to 5.8 wt. % are observed in many instances, suggesting a degree of interaction with a trapped interstitial liquid, due to the incompatible behaviour of Ti^{4+} in these systems (Roeder & Campbell, 1985; Scowen *et al*.1991;

Barnes & Roeder, 2001; Wijbrans *et al*., 2015). The unit boundary (7-8 and 11-12) seams described by O'Driscoll *et al*. (2010) also have Cr-spinel with low TiO_2 contents (< 1 wt. %), with higher concentrations observed in accessory Cr-spinel in anorthosite and troctolite that were interpreted as reflecting a trapped liquid effect (see also Lenaz *et al*., 2011). This lends support to the mineral compositional patters illustrated in Figure 14 being imposed at the postcumulus stage, suggesting at least some mobility of interstitial melt in the crystal mush.

Preferential assimilation of a peridotite cumulate

The chemistry of the Cr-spinel seams and textural analysis suggest that seams formed *in situ* within a crystal mush. The spatial relationship of Cr-spinel seams with intrusive harrisite also strongly suggests a co-genetic relationship, i.e., the intrusion of picrite caused a seam-forming reaction with the host cumulate. This is not a new concept as the interaction of picritic liquid and a more evolved component (cumulate or liquid) has been used to explain the formation of Cr-spinel horizons in many layered intrusions (e.g., Muskox; Irvine, 1977; Rum; O'Driscoll *et al*., 2010; Bushveld; Latypov *et al*., 2015). The presence and field relations of potholes, culminations, and cumulate autoliths led O'Driscoll *et al*. (2010) to suggest that Cr-spinel seams occurring between Unit 7-8 and 11-12 of the Rum ELI formed from the assimilation of feldspathic cumulate floor by the influx of picritic magma, creating a hybrid liquid capable of crystallising abundant Cr-spinel. Similar interpretations exist for the Merensky Reef of the Bushveld Complex (Ballhaus & Sylvester, 2000; Latypov *et al*., 2015).

The presence of troctolite and granular-textured peridotite autoliths in the Unit 10 peridotite (e.g., Fig. 4a) suggest that the replenishing magma was capable of reworking (i.e., assimilating) cumulate. However, the lack of feldspathic cumulate within the Unit 10 peridotite poses a problem for the application of exactly the same model to explain chromitite seams here. Previous studies (referred to above) on the Rum chromitites invoke the almost total assimilation of cumulate adjacent to the replenished magma (O'Driscoll *et al*., 2010; Latypov *et al*., 2015). However, it is not immediately obvious that this should be the outcome where picrite is emplaced into a peridotitic host. The critical point, as outlined below, is that the rocks that have traditionally been referred to as peridotite on Rum can contain up to 50 vol.% plagioclase feldspar, so are effectively melatroctolites.

In Figure 16, the invading magma (M_1) is taken as the Rum parental magma of Upton *et al*. (2002) and Holness *et al*. (2007b), equivalent to an aphyric 'M9' picrite. The assimilation of > 60% troctolite (T_1) as suggested by O'Driscoll *et al*. (2009a), labelled T_1, results in a binary mixing line with the liquid entering the spinel field thus crystallising abundant Cr-spinel. However, there is no evidence that troctolite was ever abundant enough within the Unit 10 peridotite to account for the number of seams present. The total assimilation of feldspathic peridotite of Unit 10, one of the composition of a typical granular-textured peridotite with > 70% olivine, 25% plagioclase, and 5% clinopyroxene (P_1), and a second harrisitic peridotite with 50% olivine, 45% plagioclase, and 5% clinopyroxene (P_2), by the M_1 picrite, even if possible, would fail to reach the spinel field as the percentage of olivine is too high in the assimilant. Mixing of picrite with an evolved liquid was proposed in the Muskox Intrusion by Irvine (1977). To facilitate such a mixing model on Rum, the picritic liquid would have to hybridise with the intercumulus liquid between cumulus olivine crystals in the peridotite mush. The liquid having crystallised olivine as it cools will lie on the An-Fo cotectic, or potentially at the An-Fo-Di eutectic (E). However, the hybridization of the picritic liquid and evolved intercumulus liquid on a simple binary mixing line will not move into the spinel field, so it is difficult to see how a seam will form. To satisfy the phase relations, we propose that the invading liquid reacts with the feldspathic peridotite, dissolving out plagioclase and removing only minor amounts of olivine. Such a reaction would saturate the liquid in Fo and An, and place it on the An-Fo cotectic. Continued dissolution of olivine and plagioclase might lead to the liquid attaining the peritectic point (P) at about 1317 °C (Morse, 1980), such that the reaction Fo + An produces Sp + L. The liquid may then leave the Fo-An-Di plane completely, toward SiO_2, producing spinel as it does so. The process describe above is consistent with petrographic observations, where cores of relatively sodic plagioclase crystals exist within anorthitic plagioclase oikocrysts (Fig 15b), and corroded olivine embayments are filled with Cr-spinel (Fig 6e), suggesting stronger dissolution of plagioclase than olivine within the mush. The Cr required to form abundant Cr-spinel during this reaction can potentially be sourced from the invading picrite with ~2400 ppm Cr (O'Driscoll *et al*., 2009b). The Cr-spinel forming reaction is broadly isenthalpic (*cf*. Kelemen, 1990), though the temperature difference between fresh picrite magma and of that of a peridotite mush that has already crystallised abundant plagioclase will likely result in a net

reduction in temperature. This net reduction may drive the hybrid liquid into the spinel field, permitting abundant Cr-spinel crystallisation, without the need to subsequently cool the superheated magma on hybridization (Latypov *et al*., 2015). As the Cr-spinel seams typically contain plagioclase as the intercumulus phase, the liquid path can be estimated to have descended onto the An + Sp cotectic and not the Fo + Sp cotectic (O'Driscoll *et al*., 2009a; 2010; Latypov *et al*., 2015). If the latter was the case, corroded cumulus olivine might be expected to recrystallise and new growth on olivine rims might act to 'heal' olivine crystal embayments observed ubiquitously within the Cr-spinel seams. It is also worth noting in this regard that olivine occurs interstitially to Cr-spinel seam hosted in troctolite or anorthosite (e.g., the subsidiary Cr-spinel seams at the Unit 7-8 boundary (O'Driscoll *et al*., 2007a). Finally, it should be noted that the Cr abundance has been shown to affect the spinel stability field (Irvine, 1977), and that our use of the An-Fo-Di ternary diagram is simply a visual aid to illustrate the proposed reaction.

The preferential dissolution of phases in harzburgite has been used to explain the presence of dunitic bodies within the upper mantle sections of ophiolites (Quick, 1981; Kelemen, 1990; Kelemen *et al*., 1995; Morgan & Liang, 2005). Picritic/basaltic liquid saturated in olivine successively dissolves clino- and orthopyroxene in lherzolites and harzburgites, crystallising olivine to produce dunite residue with similar Mg# of olivine to the surrounding harzburgite (Quick, 1981; Kelemen, 1990; Kelemen *et al*., 1995). Processes invoking the removal of lower temperature phases by magma have also been proposed for the Rum ELI to produce cpx-poor troctolite from gabbroic rocks (Holness *et al*., 2007b; Leuthold *et al*., 2014). Furthermore, this process has also been linked to the formation of chromitites found in dunites within the upper mantle (see Gonzaléz-Jiménez *et al*., 2014). Experimental work by Donaldson (1985) on the dissolution rates of common minerals within basaltic magmas showed that plagioclase will dissolve out of the rock faster than olivine at a rate of ~86 μm/hour. The dominant control of this process is the requirement for the dissolving magma to be undersaturated in the mineral being dissolved (Donaldson, 1985). It seems possible therefore that the picritic magma intruded into the crystal mush is more than capable of preferentially dissolving intercumulus plagioclase, producing a hybrid liquid able to crystallise abundant Cr-spinel within an existing crystal framework of olivine, without removing significant portions of olivine.

Hot tearing of the crystal mush as a mechanism for harrisite intrusion and Cr-spinel seam formation

Hot tearing is a metallurgic phenomenon that occurs during the casting of Al-alloys, where tears open as a result of thermal contraction parallel to the walls of the mould and to the solidification front that fill with the inter-crystalline liquid. This process of ductile fracturing is an intergranular or interdendritic process occurring above the solidus, i.e., in a semi-solid state (Lahaie & Bouchard, 2001; Eskin et al. 2004). Hot tearing has been shown to operate when the alloy consists of a touching framework of crystals and an interstitial liquid at high solid fractions, up to 85–95% (Eskin *et al*. 2004). Many of fundamental features of hot tearing are applicable to natural silicate crystal mushes, and have been used to describe the origins of a variety of preferentially oriented segregation structures in flood basalt feeders (Phillpotts *et al*. 1996), dykes and sills (Geshi, 2001; Marsh, 2002), migmatites and granitic melts (Vigneresse *et al*. 1996), and layered mafic intrusions (Humphreys & Holness, 2013; Namur et al., 2013). In these studies, the crystal mush is 'torn' by local stresses produced by compaction, differential cooling, gravitational sagging, or localised shear, forming tears that allow the accumulation of liquid. Once the dilation has opened, liquid is preferentially drawn to the lower stress tears where it crystallises, producing texturally distinct schlieren or pods. Humphreys & Holness (2013) proposed that this process occurred in crystal mushes in the Marginal Border Series of the Skaergaard Intrusion, Greenland. The solidification front of the Marginal Border Series was vertically-oriented and the crystal mush was essentially unsupported towards the centre of the magma chamber; this produced a strong lateral pulling stress (σ_3), with little to no vertical (i.e., compaction) stress (σ_1) as the crystal mush was effectively pulled towards the main magma body from the sidewall of the chamber. The gravitational stress on the mush facilitated shearing, opening tears in highly crystalline mushy rocks that filled with liquid drawn in from the main magma body, producing textural and chemically variable segregations oriented parallel to the shearing direction.

Shearing and hot tearing in the Unit 10 peridotite

Gravitational collapse or sagging of crystal mush as a mechanism to form hot tears might be important in the RLS, given the abundant evidence for deformation there (e.g., Volker & Upton, 1990; Emeleus *et al*. 1996; O'Driscoll et al. 2007b; Troll & Emeleus, 2014). The RLS has a roughly bowl shaped structure, with the layers dipping variably towards the Long Loch Fault feeder zone (Fig. 1). Significant syn-magmatic deformation structures with proximity to this feeder zone suggest contemporaneous deformation and 'sagging' of the mush into the feeder zone (Volker & Upton, 1990; Emeleus *et al*., 1996; Troll & Emeleus, 2014). Magnetic fabrics within the ELI, including the Unit 10 peridotite, support this view (O'Driscoll *et al*. 2007b). Fundamentally, this sagging may have resulted in a significant $\sigma_3 > \sigma_1$ stress that strengthened towards the Long Loch Fault, where evidence for deformation is greatest (e.g., Volker & Upton, 1990). This strong σ_3 pulling stress has the potential to create shearing of the mush, and if the crystallinity is high, can open dilations and hot tears, allowing magma to be drawn up to low stress regions.

Peridotites in Unit 10 are largely classic orthocumulates (Wager et al, 1960) and resemble the ideal intergranular semi-solid configuration of Lahaie & Bouchard (2001), with a loosely touching crystal framework surrounded by a film of liquid (i.e., plagioclase-clinopyroxene normative liquid). Olivine is assumed to have been present at the time of intrusion (see earlier discussion), providing a minimum crystallinity (ϕ) estimate of 75–85% (calculated from *ImageJ*). Relic plagioclase crystals contributes < 1% to the assumed crystallinity at the time of intrusion, however, if Cr-spinel is taken to reflect the presence of pre-existing plagioclase (which has been assimilated) crystallinity could be as high at ~95%. It is important to note that the process of hot tearing requires only a thin film of liquid to exist around crystals to operate (Lahaie & Bouchard, 2001), and that at high crystallinities in orthocumulates would not immediately constitute a rigid framework, particularly where the crystals are equant. The quantification of tensile strength of the crystal mush and the potential for hot tearing is poorly constrained by the paucity of experimental data for the mechanical properties of mushy crystalline rocks. Marsh (2002) proposed a quantitative estimate of the tensile strength of molten-to-solidified basaltic rock approximated as a function of crystallinity (ϕ):

$$\sigma_s = \sigma_0 \left[\frac{\sigma_f}{\sigma_0}\right]^{((\Phi-\Phi_0)/(1-\Phi_0))} \quad (1)$$

where σ_0 is the tensile strength at ϕ_0 (100% solid) and σ_f is the tensile strength on the solidus, where ϕ is 1. Marsh (2002) proposed a region of tearing and instability of a crystal mush with ϕ=65%, at a tensile strength of ~1 bar for a basaltic sill (Fig. 17). Higher crystallinities and high modal olivine within proposed sills in the Unit 10 peridotite would point to a greater tensile strength of the mush, suggesting the region proposed is potentially a minimum estimate, with tearing occurring into higher crystallinities (Fig. 17). The common feature of hot tearing models is the requirement for high crystallinities, greater than ~60% when the mush gains competency (Lahaie & Bouchard, 2001; Marsh, 2002; Eskin *et al*. 2004; Marsh, 2013). The RLS was emplaced at < 1 km depth which approximates to 150 ±50 bar (Holness, 1999), suggesting only negligible vertical stress (σ_1) from lithostatic pressure, and a relatively thin cumulate pile above Unit 10 (~100 m) that would have been significantly less than the lateral stress produced by the sagging of up to 95 m thick Unit 10 crystal mush across a distance of ~6 km towards the Long Loch feeder. As the mush is unlikely to be solidifying at a constant rate (particularly if being intruded repeatedly by picrite), it will produce a largely random intrusive pattern, and not bottom to top as is commonly assumed for layered intrusions. The concept of a variable solidification rate throughout is important for shear localisation between more rigid and mushy cumulate (Geshi, 2001). Localised shear zones at the boundaries of two rheologically contrasting materials may generate foliation, which is commonly observed at the boundaries between variable peridotite types and Cr-spinel seams in the Unit 10 peridotite (e.g., Fig. 6c). Indeed, the generation of non-equant crystal habits (e.g., elongate crystals in Unit 10) aids rigidity and susceptibility to tearing (Vigneresse et al, 1996), which could help to explain the close spatial relationship between stronger olivine foliations and intrusive peridotites (and Cr-spinel seams). The fundamental requirements for this type of tearing to occur in the Unit 10 peridotite are qualitatively met and point to a potentially prevalent process during the incremental development of the crystal mush, with important implications for the formation of harrisite layers and their associated Cr-spinel seams.

Conceptual Model

The key processes in the formation of the Unit 10 peridotite discussed in this section are summarised in Figure 18. We envisage a scenario in which a strong $\sigma_3 > \sigma_1$ stress-field promoted by sagging of the crystal mush towards the Long Loch Fault feeder zone caused gravitational collapse and 'hot tearing' parallel to σ_3. This shearing stress of the crystal mush created intergranular dilations and shear zones, facilitating the migration of magma to zones of lower stress, producing peridotite layers (particularly harrisite) and Cr-spinel seams within the mush. These dilations likely amalgamated during the formation (akin to fault formation), producing extended pathways for invading magma (as evidenced by the intrusion-scale lateral correlation of harrisite layers; Figure 2), and providing the means to feed magma deep (laterally) into the mush. On entering the crystal mush along the numerous tears and dilations (Fig. 18a), the picrite magma locally assimilated feldspathic material from the mush, producing the various seam types discussed in this study. Granular-textured peridotite hosted seams therefore represent the injection of picrite into the mush where the intruded picrite did not inflate into a definitive sill (Fig. 18b), while boundary type seams represent intrusion of picrite which has inflated into a sill (e.g., harrisites; Fig. 18c). Intra-harrisite seams are interpreted to represent continued through-flow of picrite in a conduit, or perhaps multiple generations of through-flow, assimilating feldspathic material in the same way as in the previous examples (Fig. 18c).

Reactive liquid flow within the crystal mush: compositional disequilibrium of intercumulus plagioclase

An important consequence of the repeated injection of primitive magma into a crystal mush is the potential for the displacement of existing intercumulus liquids and/or the partial removal, via dissolution, of cumulus and intercumulus solids. The ubiquitous occurrence of zoning in intercumulus plagioclase oikocrysts reported in this study strongly supports the movement of reactive liquids in the Unit 10 peridotite, resulting in local compositional disequilibrium within the crystal mush. Published work on chemical and isotopic zoning in cumulate rocks has generally focused on cumulus plagioclase in feldspathic cumulates, with variable mechanisms used to explain the chemical disequilibrium, such as compaction and liquid migration (Humphreys, 2009; Namur & Charlier, 2012), diffusion-controlled redox and electrochemical gradients (Veksler *et al.*, 2015), or reworking

and redeposition of crystals of different origins in density currents or plumes (Tepley & Davidson, 2003). Recent studies of reactive melt flow caused by the intrusion of the Unit 9 peridotite in the ELI suggest that chemical disequilibrium can be induced by migrating melts and can be recorded in zoning of clinopyroxene oikocrysts (Leuthold *et al*., 2014). Because intercumulus phases represent crystallised interstitial melt, zoning in these crystals is likely to be a function of processes operating within the crystal mush. The Unit 10 peridotite commonly displays compositional zonation of intercumulus plagioclase, especially close to Cr-spinel seams (Fig. 6a, b; 7; 15). The zoning patterns may be normal, reverse, or oscillatory. Normal zoning of intercumulus plagioclase has also been reported from peridotites in Unit 9, 12 and 14 (Holness, 2005; Holness *et al*., 2007b; Holness & Winpenny, 2008).

The Unit 9 intrusive model is a useful analogy for the interpretation of the Unit 10 peridotite presented here. For example, the idea that reactive intercumulus melts can be displaced into the overlying crystal mush has already been proposed for Rum (Holness *et al*., 2007; Leuthold *et al*., 2014). Reversely-zoned intercumulus plagioclase oikocrysts within Cr-spinel seams can be explained by the injection of picritic magma, assimilation of existing plagioclase in the peridotite host, and subsequent recrystallization of more calcic plagioclase together with Cr-spinel around the olivine framework. Low-anorthite plagioclase cores remain where assimilation was incomplete (Fig. 15b). Normally-zoned plagioclase in intercumulus plagioclase is also found just above the limits of a Cr-spinel seam located on the upper surface of a harrisite layer (Fig 15c). Here, the injection of picritic magma may have locally displaced evolved intercumulus liquid into the overlying mush, producing low-anorthite rims onto the crystallising plagioclase. The evidence provided by the coupled occurrence of Cr-spinel seams and zoned intercumulus plagioclase (including oscillatory zoning) indicates that this process of injection (with coupled assimilation and displacement) occurred repeatedly throughout the formation of the Unit 10 peridotite (see Fig. 18c).

The Upper Peridotite: a pre-existing crystal mush?

As described above, the Unit 10 peridotite can be subdivided into two texturally and chemically distinct portions (Fig. 2). Palacz & Tait (1985) were the first to recognise the two (upper and lower)

peridotite bodies and initially separated them at ~40 m based on an abrupt textural change. The detailed logging carried out in this study has confirmed the same textural change at this stratigraphic height, matching the previous authors' original demarcation well. Palacz & Tait (1985) and Tait (1985) reported more Fe-rich olivine in the UP than in the LP (>Fo_{85} versus $Fo_{80–83}$, respectively) which we also find in our study. They also noted a textural change in olivine, to more tabular crystals and a distinct increase in the abundance of intercumulus clinopyroxene. Palacz & Tait (1985) also noted a change in $^{87}Sr/^{86}Sr$ ratios (Fig 19), with the UP being more radiogenic than the LP (average values ~0.7050 and ~0.7031, respectively). They attributed these changes, particularly the distinct isotopic difference between the UP and LP, to crystallisation from two separate parental magma bodies.

The boundary between the LP to the UP is marked by a harrisite layer, a textural change in olivine, an increase in intercumulus proportion, and clinopyroxene oikocrysts that also become more abundant. However, the appearance of clinopyroxene across the LP-UP boundary is gradational, and the lowermost three metres of the UP has much lower clinopyroxene modal abundances than above this point, ~10% versus 30%, respectively (Fig. 3e). The compositions of disseminated Cr-spinel also change significantly, as compared with the LP, with the most Fe^{3+} enriched compositions and consistently high TiO_2 values found in the UP (Figure 14). This is consistent with Cr-spinel compositions that are more modified from the primary Al-rich Cr-spinel (O'Driscoll *et al*., 2009a; 2010; Leuthold *et al*., 2015).

Holness *et al*. (2007b) argued that the intrusion of the Unit 9 peridotite created a metasomatic marker horizon where a gabbroic crystal mush was partially melted, removing pyroxene from this section and recrystallizing it further up section. Leuthold *et al*. (2014) showed a similar relationship, showing that the displaced intercumulus melt was capable of further metasomatic alteration of the mush, creating highly pyroxene-rich gabbros in the final stage of this 'reactive liquid flow'. The observed change in clinopyroxene abundance and compositional modification of Cr-spinel fit with this model very well, suggesting that the intrusion of the LP potentially caused partial melting of the lowermost UP, removing pyroxene and causing significant modification of Cr-spinel by reaction with interstitial liquids. This bears lots of similarities to recent interpretations of the Unit 9 peridotite

(Holness *et al*., 2007b; Leuthold *et al*., 2014). Zoning of intercumulus plagioclase is also observed in the UP, suggesting a form of infiltration metasomatism or reactive liquid flow was capable of causing localised compositional disequilibrium similar to what has been found the LP. The clinopyroxene oikocrysts of the Unit 10 UP are also compositionally zoned (Fig. 15d), a feature reported by Leuthold et al. (2014) from within the Unit 9 feldspathic cumulate and attributed to reactive melt flow in the crystal mush.

The Sr isotopic variation found by Palacz & Tait (1985) further support these points. The lowermost portion of the UP is isotopically ($^{87}Sr/^{86}Sr$) similar to the LP (Fig. 19), and as Sr is hosted almost entirely in intercumulus plagioclase and clinopyroxene (Tepley & Davidson, 2003), partial melting of these phases by less radiogenic liquid from the intrusion of the LP would drastically alter the $^{87}Sr/^{86}Sr$ ratios of the UP mineralogy, an idea also discussed for parts of the Unit 9 feldspathic cumulate (Leuthold *et al*., 2014). The stepped isotopic variation manifested at the boundary between the LP and the UP (Fig. 19) precludes their formation via fractionation of the same source magma, as suggested already by Palacz & Tait (1985). It seems clear that the Unit 10 feldspathic cumulate is formed from a magma containing much more radiogenic Sr than anything observed in the LP (Palacz, 1984).

The removal of clinopyroxene from the crystal mush implies almost complete crystallisation of the protolith; as this phase is a eutectic crystallisation product (Fig. 16). Harrisite is rare in the UP, but 'hopper harrisite' layers are present, occurring as non-layer parallel sheets (Fig. 4h), and pegmatites are markedly more abundant than in the LP, also occurring as non-layer parallel sheets. Non-planarity of layers' points to a crystal mush that is also almost completely solidified, where shearing was limited or absent due to the rigidity of the mush, producing no easy pathway for infiltrating magma to migrate along (Fig. 18).

While the timing of emplacement between the UP and overlying feldspathic cumulate is not certain, the discussion above could be used to make the case for the UP being present at the time of emplacement of the LP. This would add further support to our argument for Unit 10 as an incrementally developed crystal mush, and would also imply that layered intrusion cumulate sequences do not have to be constructed from the bottom-up.

Platinum-group element (PGE) enrichment

Cr-spinel seams in the Unit 10 peridotite contain base-metal sulphides, which are ubiquitously associated with a diverse array of PGM and Au-Ag grains (e.g., Fig. 7; 8). The Unit 10 Cr-spinel seams exhibit PGE enrichment up to 130 ppb Pd and 100 ppb Pt (O'Driscoll unpublished data). Like the formation of Cr-spinel seams, PGE enrichment raises a mass-balance problem, as the thickness of many harrisite layers (< 1 m) is insufficient to account for the Cr concentrations in the seams and of 100's ppb levels of PGE-enrichment. To account for this problem in much larger layered intrusions, models have been forwarded that envisage the PGE being scavenged from a thick column of magma (Campbell *et al*. 1983; Cawthorn *et al*., 2005). Where *in situ* crystallisation of the PGM has been proposed, vigorous convection of a standing body of magma was invoked to allow the base-metal sulphides to scavenge PGE from the melt as it convects over the magma-crystal mush interface (Latypov *et al*., 2013). Many of the harrisite sheets are probably not thick enough to allow for vigorous convection (*cf.* O'Driscoll *et al*., 2010; Latypov *et al*., 2013; Latypov *et al*., 2015). However, the mass-balance issue can be solved by continual lateral through-flow within picrite sills where many times the volume of magma has passed through the sill than is currently represented by the solidified harrisite. This has important economic implications for comparatively thin cumulate bodies that are anomalously rich in PGEs and other precious metal mineralisation in other layered intrusions. Examples include the Cr-spinel lined peridotite sills below the platiniferous Merensky Reef of the Bushveld Complex (Ballhaus, 1988; Latypov *et al*. 2015), where replenishment and PGE-enrichment have plausibly occurred within the crystal mush. Similarities between textures of Rum peridotite-hosted Cr-spinel seams and the PGE-bearing peridotite-hosted chromitites of the Ultramafic Series of the Stillwater Complex (see Jackson, 1961) are also a potential analogue, where the ideas proposed here could be applied.

CONCLUSIONS

Recent work on the RLS, particularly the ELI has found growing evidence that argues against traditional models of crystal settling for fractionating discrete magma batches. Following the classic

work of Brown (1956), it was suggested as early as 1988 (Bédard *et al*., 1988) that many of the peridotite layers that make up the ELI formed by injection of magma into a pre-existing crystal mush. In this study, we present further evidence to support this view and conclude that the Unit 10 peridotite was developed incrementally by numerous, small volume replenishment events into a pre-existing, and partially consolidated crystal mush undergoing significant shear stress by gravitational sagging toward the feeder. The importance of this conclusion is highlighted by the fact that Unit 10 has stood as the type example of batch fractionation on Rum for more than 50 years. The repeated intrusive replenishment of picritic magma crystallised harrisitic and granular-textured peridotite, the former generating significant liquid displacement structures. Closely associated diffuse Cr-spinel seams that occur along the base, top, and interior of these peridotites crystallised *in situ* on intrusion of this magma as a product of a preferential assimilation reaction with peridotitic cumulate. Repeated intrusion of picritic magma into the crystal mush generated localised compositional disequilibrium in silicate phases adjacent to Cr-spinel seams by the displacement and replacement of intercumulus liquids and solids. This model has important local implications for other Cr-spinel seam bearing peridotite bodies such as Units 8 and 12 (Henderson, 1975; O'Driscoll *et al*., 2010), where the peridotite may have undergone small volume intrusive replenishment.

As the Rum Western Layered Intrusion contains the greatest abundance of harrisite and also numerous Cr-spinel seams (Wadsworth, 1961), the applicability of the model presented here has relevance for other portions of the RLS. There is also scope to draw parallels with much larger layered intrusions such as the Ultramafic Series of the Stillwater Complex (Montana), where thick and similarly-textured Cr-spinel seams occur hosted within peridotite (Jackson, 1961). Finally, given that the Unit 10 Cr-spinel seams contain PGE, there is economic implications for world class PGE ore deposits in layered intrusions such as the Bushveld Complex, South Africa, where models of intrusive replenishment have not yet been fully explored.

ACKNOWLEDGEMENTS

Scottish National Heritage (SNH) is thanked for sampling permission during 2014 and 2015. Peter Greatbatch and David Wilde (Keele University) are thanked for excellent thin-section preparation.

Hazel Horsch and Alan Butcher are thanked for their assistance generating the QEMSCAN images. Andreas Kronz and Gregor Breedveld are thanked for assistance with electron-microprobe analysis at the University of Göttingen. Rais Latypov, Stephen Barnes, and Julien Leuthold are thanked for very constructive and thoughtful reviews which greatly improved the clarity and focus of the manuscript. Marjorie Wilson is also thanked for careful editorial handling.

FUNDING

LNH acknowledges funding from a Natural Environmental Research Council (NERC) Studentship [grant number: 1361482] and Keele University, and also from the Institute of Materials Minerals and Mining (IoM^3) Edgar Pam Fellowship for whole rock analysis. J.S.D. was supported by a UCD Funding Grant and by Science Foundation Ireland Grant No. 13/RC/2092, which is co-funded under the European Regional Development Fund.

REFERENCES

Ballhaus, C. (1988). Potholes of the Merensky reef at Branspruit shaft, Rustenburg platinum mines; primary disturbances in the magmatic stratigraphy. *Economic Geology* **83**, 1140–1158

Ballhaus, C. & Sylvester, P. (2000). Noble Metal Enrichment Processes in the Merensky Reef, Bushveld Complex. *Journal of Petrology* **41**, 545–561.

Barnes, S. & Jones, S. (2013). Deformed Chromitite Layers in the Coobina Intrusion, Pilbara Craton, Western Australia. *Economic Geology* **108**, 337–354

Barnes, S.J. & Roeder, P.L. (2001). The Range of Spinel Compositions in Terrestrial Mafic and Ultramafic Rocks. *Journal of Petrology* **42**, 2279–2302

Bédard, J. H., Sparks, R. S. J., Renner, R., Cheadle, M. J. & Hallworth, M. A. (1988). Peridotite sills and metasomatic gabbros in the Eastern Layered Series of the Rhum Complex. *Journal of the Geological Society, London* **145**, 207–224

Bell, B.R. & Claydon, R.V. (1992). The cumulus and post-cumulus evolution of chrome-spinels in ultrabasic layered intrusions: evidence from the Cuillin Igneous Complex, Isle of Skye, Scotland. *Contributions to Mineralogy and Petrology* **112**, 242–253

Boorman, S., Boudreau, A. & Kruger, F.J. (2004). The Lower Zone–Critical Zone transition of the Bushveld Complex: a quantitative textural study. *Journal of Petrology* **45**, 1209–1235

Butcher, A.R., Pirrie, D., Prichard, H.N. & Fisher, P. (1999). Platinum-group mineralisation in the Rum layered suite, Scottish Hebrides, UK. *Journal of the Geological Society, London* **156**, 213–216

Brown, G.M. (1956). The layered ultrabasic rocks of Rhum, Inner Hebrides. *Philosophical Transactions of the Royal Society of London Series B* **668**, 1–53

Campbell, I.H. & Murck, B.W. (1993). Petrology of the G and H Chromitites Zones in the Mountain View Area of the Stillwater Complex, Montana. *Journal of Petrology* **34**, 291–316

Campbell, I.H., Naldrett, A.J. & Barnes, S.J. (1983). A Model for the Origin of the Platinum-Rich Sulfide Horizons in the Bushveld and Stillwater Complexes. *Journal of Petrology* **24**, 133–165.

Cashman, K.V. & Marsh, B.D. (1988). Crystal size distribution (CSD) in rocks and the kinetics and dynamics of crystallisation II. Makaopuhi lava lake. *Contributions to Mineralogy and Petrology* **99**, 292–305

Cawthorn, R.G. (2005). Pressure fluctuations and the formation of the PGE-rich Merensky and chromitite reefs, Bushveld Complex. *Mineralium Deposita* **40**, 231–235

Donaldson, C.H. (1974). Olivine Crystal Types in Harrisitic Rocks of the Rhum Pluton and in Archaean Spinifex Rocks. *Geological Society of America Bulletin* **85**, 1721–1726

Donaldson, C.H. (1975). A petrogenetic study of harrisite in the Isle of Rhum pluton, Scotland. *Unpublished PhD Thesis, University of St. Andrews*

Donaldson, C.H. (1976). An Experimental Investigation of Olivine Morphology. *Contributions to Mineralogy and Petrology* **57**, 187–213

Donaldson, C.H. (1982). Origin of some of the Rhum harrisite by segregation of intercumulus liquid. *Mineralogical Magazine* **45**, 201–209

Donaldson, C.H. (1985). The rates of dissolution of olivine, plagioclase and quartz in a basaltic melt. *Mineralogical Magazine* **49**, 683–693

Droop, G.T.R. (1987). A general equation for estimating Fe^{3+} concentrations in ferromagnesian silicates and oxides from microprobe analyses using stoichiometric criteria. *Mineralogical Magazine* **51**, 431–435

Dunham, A.C. & Wadsworth, W.J. (1978). Cryptic variation in the Rhum layered intrusion. *Mineralogical Magazine* **42**, 347–356

Emeleus, C.H. (1994). Rum solid geology map 1:20000. Scottish Natural Heritage

Emeleus, C.H. & Bell, B.R. (2005). British Regional Geology: the Palaeogene Volcanic Districts of Scotland. (4th Ed). Keyworth: British Geological Survey

Emeleus, C.H., Cheadle, M.J., Hunter, R.H., Upton, B.G.J. & Wadsworth, W.J. (1996). The Rum Layered suite. In: Cawthorn, R.G (ed). *Layered igneous rocks. Developments in petrology*, vol 15, Elsevier Science BV: Amsterdam, 404–440

Emeleus. C.H. & Troll, V.R. (2014). The Rum Igneous Centre, Scotland. *Mineralogical Magazine* **78**, 805–839

Eskin, D.G., Suyitno. & Katgerman, L. (2004). Mechanical properties in the semi-solid state and hot tearing of aluminium alloys. *Progress in Materials Science* **49**, 629–711.

Faure, F., Trolliard, G., Nicollet, C. & Montel, J-M. (2003)..A developmental model of the olivine morphology as a function of the cooling rate and the degree of undercooling. *Contributions to Mineralogy and Petrology* **145**, 251–263

Geshi, N. (2001). Melt segregation by localized sear deformation and fracturing during crystallization of magma in shallow intrusions of the Otoge volcanic complex, central Japan. *Journal of Volcanology and Geothermal Research*, **106**, 285–300.

González-Jiménez, J.M., Griffin, W.L., Proenza, J.A., Gervilla, F., O'Reilly, S.Y., Akbulut, M., Pearson, N.J. & Arai, S. (2014). Chromitites in ophiolites: How, where, when, why? Part II. The crystallization of chromitites. *Lithos* **189**, 140–158

Hamilton, M.A., Pearson, D.G., Thompson, R.N., Kelley, S.P. & Emeleus, C.H. (1998). Rapid eruption of Skye lavas inferred from precise U–Pb and Ar–Ar dating of the Rum and Cuillin plutonic complexes. *Nature* **394**, 260–263

Harker, A. (1908). The Geology of the Small Isles of Inverness-shire. Memoir of the Geological Survey of Scotland

Henderson, P. (1975). Reaction trends shown by chrome-spinels of the Rhum layered intrusion. *Geochimica et Cosmochimica Acta* **39**, 1035-1044

Henderson, P. & Suddaby, P. (1971). The Nature and Origin of the Chrome-Spinel of the Rhum Layered Intrusion. *Contributions to Mineralogy and Petrology* **33**, 21–31

Humphreys, M.C.S. (2009). Chemical Evolution of Intercumulus Liquid, as Recorded in Plagioclase Overgrowth Rims from the Skaergaard Intrusion. *Journal of Petrology* **50**, 127–145

Humphreys, M.C.S, & Holness, M.B. (2010). Melt-rich segregations in the Skaergaard Marginal Border Series: Tearing of a vertical silicate mush. *Lithos* **119**, 181–192

Higgins, M.D. (1994). Numerical modelling of crystal shapes in thin-sections; estimation of crystal habit and true size. *American Mineralogist* **79**, 113–119

Higgins, M.D. (2002a). Closure in crystal size distributions (CSD), verification of CSD calculations, and the significance of CSD fans. *American Mineralogist* **81**, 171–175

Higgins, M.D. (2002b). A crystal size-distribution study of the Kiglapait layered mafic intrusion, Labrador, Canada: evidence for textural coarsening. *Contributions to Mineralogy and Petrology* **144**, 314–330

Higgins, M.D. (2006). *Quantitative textural measurements in igneous and metamorphic petrology*: Cambridge, Cambridge University Press, UK

Higgins, M.D. (2000). Measurement of Crystal Size Distributions. *American Mineralogist* **85**, 1105–1116

Holness, M.B. (1999). Contact metamorphism and anataxis of Torridonian arkose by minor intrusions of the Rum Igneous Complex, Inner Hebrides, Scotland. *Geological Magazine* **136** (5), 527–542.

Holness, M.B. (2005). Spatial Constraints on Magma Chamber Replenishment Events from Textural Observations of Cumulates: the Rum Layered Intrusion, Scotland. *Journal of Petrology* **46**, 1585–1601

Holness, M.B. (2007a). Textural immaturity of cumulates as an indicator of magma chamber processes: infiltration and crystal accumulation in the Rum Eastern Layered Intrusion. *Journal of the Geological Society, London* **164**, 529–539

Holness, M.B., Hallworth, M.A., Woods, A. & Sides, R.E. (2007b). Infiltration Metasomatism of Cumulates by Intrusive Magma Replenishment: the Wavy Horizon, Isle of Rum, Scotland. *Journal of Petrology* **48**, 563–587

Holness, M.B. & Winpenny, B. (2008). The Unit 12 allivalite, Eastern Layered Intrusion, Isle of Rum: a textural and geochemical study of an open-system magma chamber. *Geological Magazine* **146**, 437–450

Houlé, M.G., Préfontaine, S., Fowler, A.D. & Gibson, H.L. (2009). Endogeneous growth in channelized komatiite lava flows: evidence from spinifex-textured sills at Pyke Hill and Serpentine Mountain, Western Abitibi Greenstone Belt, Northeastern Ontario, Canada. *Bulletin of Volcanology* **71**, 881–901.

Irvine, T.N. (1977). Origin of chromitite layers in the Muskox intrusion and other stratiform intrusions: A new interpretation. *Geology* **5**, 273–277

Jackson, E.D. (1961). Primary Textures and Mineral Associations in the Ultramafic Zone of the Stillwater Complex, Montana. *Geological Survey Professional Paper* **358**

Junge, M., Oberthür, T. & Melcher, F. (2014). Cryptic variation of chromite chemistry, platinum group element and platinum group mineral distribution in the UG-2 chromitite: an example from the Karee mine, western Bushveld Complex, South Africa. *Economic Geology* **109**, 795–810

Kelemen, P. (1990). Reaction Between Ultramafic Rock and Fractionating Basaltic Magma I. Phase Relations, the Origin of Calc-alkaline Magma Series, and the Formation of Discordant Dunite. *Journal of Petrology* **31** (1), 51–98

Kelemen, P., Shimizu, N. & Salters, V.J.M. (1995). Extraction of mid-ocean-ridge basalt from the upwelling mantle by focused flow of melt in dunite channels. *Nature* **375**, 747–753

Lahaie, D.J. & Bouchard, M. (2001). Physical Modelling of the Deformation Mechanisms of Semisolid Bodies and a Mechanical Criterion for Hot Tearing. *Metallurgical and Materials Transactions B.* **32**, 697–705.

Latypov, R., Chistyakova, S., Page, A. & Hornsey, R. (2015). Field evidence for the *in situ* crystallisation of the Merensky Reef. *Journal of Petrology* **56**, 2341–2372

Latypov, R., O'Driscoll, B. & Lavrenchuk, A. (2013). Towards a model for the in situ origin of PGE reefs in layered intrusions: insights from chromitite seams of the Rum Eastern Layered Intrusion, Scotland. *Contributions to Mineralogy and Petrology* **166**, 309–327

Lenaz, D., O'Driscoll, B. & Princivalle, F. (2011). Petrology of the anorthosite-chromitite seam association: crystal-chemical and petrological insights from the Rum Layered Suite, NW Scotland. *Contributions to Mineralogy and Petrology* **162**, 1201–1213

Leuthold, J., Blundy, J.D. & Brooker, R.A. (2015). Experimental petrology constraints on the recycling of mafic cumulate: a focus on Cr-spinel from the Rum Eastern Layered Intrusion, Scotland. *Contributions to Mineralogy and Petrology* 170: 12

Leuthold, J., Blundy, J.D., Holness, M.B. & Sides, R. (2014). Successive episodes of reactive liquid flow through a layered intrusion (Unit 9, Rum Eastern Layered Intrusion, Scotland). *Contributions to Mineralogy and Petrology* **167**, 1021–1038

Lipin, B.R. (1993). Pressure Increases, the Formation of Chromite Seams, and the Development of the Ultramafic Series in the Stillwater Complex, Montana. *Journal of Petrology* **34**, 955–976

Lofgren, G.E. & Donaldson, C.H. (1975). Curved branching crystals and differentiation in comb-layered rocks. *Contributions to Mineralogy and Petrology* **49**, 309–319

Marsh, B.D. (1998). On the Interpretation of Crystal Size Distributions in Magmatic Systems. *Journal of Petrology* **39**, 553–599

Marsh, B.D. (2002). On bimodal differentiation by solidification front instability in basaltic magmas, part 1: Basic mechanics. *Geochimica et Cosmochimica Acta* **66** (12), 2211–2229.

Marsh, B.D. (2013). On some fundamentals of igneous petrology. *Contributions to Mineralogy and Petrology* **166**, 665–690.

Morse, S.A. (1980). *Basalts and phase diagrams*. Springer Verlag, New York. 493 pp

Mock, A. & Jerram, D.A. (2005). Crystal Size Distributions (CSD) in Three Dimensions: Insights from the 3D Reconstruction of a Highly Porphyritic Rhyolite. *Journal of Petrology* **46**(8), 1525–1541

Morgan, Z. & Liang, Y. (2005). An experimental and numerical study of the kinetics of harzburgite reactive dissolution with applications to dunite dike formation. *Earth and Planetary Science Letters* **214**, 59–74

Mondal, S.K. & Mathez, E.A. (2007). Origin of the UG2 chromitite seam layer, Bushveld Complex. *Journal of Petrology* **48**, 495–510

Namur, O. & Charlier, B. (2012). Efficiency of compaction and compositional convection during mafic crystal mush solidification: the Sept Iles layered intrusion, Canada. *Contributions to Mineralogy and Petrology* **163**, 1049–1068

Namur, O., Humphreys, M.C.S. & Holness, M.B. (2013). Lateral Reactive Infiltration in a Vertical Gabbroic Crystal Mush, Skaergaard Intrusion, East Greenland. *Journal of Petrology* **54**, 985–1016.

O'Driscoll, B., Butcher, A.R. & Latypov, R. (2014). New insights into precious metal enrichment on the Isle of Rum, Scotland. *Geology Today* **30**, 134–141

O'Driscoll, B., Emeleus, C.H., Donaldson, C.H. & Daly, J.S. (2010). Cr-spinel Seam Petrogenesis in the Rum Layered Suite, NW Scotland: Cumulate Assimilation and in situ Crystallisation in a Deforming Crystal Mush. *Journal of Petrology* **51**, 1171–1201

O'Driscoll, B., Donaldson, C.H., Troll, V.R., Jerram, D.A. & Emeleus, C.H. (2007a). An Origin for Harrisitic and Granular Olivine in the Rum Layered Suite, NW Scotland: a Crystal Size Distribution Study. *Journal of Petrology* **48**, 253–270

O'Driscoll, B., Hargraves, R.B., Emeleus, C.H., Troll, V.R., Donaldson, C.H. & Reavy, R.J. (2007b). Magmatic lineations inferred from anisotropy of magnetic susceptibility fabrics in Units 8, 9, and 10 of the Rum Eastern Layered Series, NW Scotland. *Lithos* **98**, 27–44

O'Driscoll, B., Donaldson, C.H., Daly, J.S. & Emeleus, C.H. (2009a). The roles of melt infiltration and cumulate assimilation in the formation of anorthosite and a Cr-spinel seam in the Rum Eastern Layered Intrusion, NW Scotland. *Lithos* **111**, 6–20

O'Driscoll, B., Day, J.M.D., Daly, J.S., Walker, R.J. & McDonough, W.F. (2009b). Rhenium–osmium isotopes and platinum-group elements in the Rum Layered Suite, Scotland: Implications for Cr-spinel seam formation and the composition of the Iceland mantle anomaly. *Earth and Planetary Science Letters* **286**, 41–51

Palacz, Z.A. (1984). Isotopic and geochemical evidence for the evolution of a cyclic unit in the Rhum intrusion, north-west Scotland. *Nature* **307**, 618–620

Palacz, Z.A. & Tait, S.R. (1985). Isotopic and geochemical investigation of unit 10 from the Eastern Layered Series of the Rhum Intrusion, Northwest Scotland. *Geological Magazine* **122**, 485–490

Philpotts, A.R., Carroll, M. & Hill, J.M. (1996). Crystal-Mush Compaction and the Origin of Pegmatitic Segregation Sheets in a Thick Flood-Basalt Flow in the Mesozoic Hartford Basin, Connecticut. *Journal of Petrology* **37**, 811–836.

Quick, J.E. (1981). The Origin and Significance of Large, Tabular Dunite Bodies in the Trinity Peridotite, Northern California. *Contributions to Mineralogy and Petrology* **78**, 413–422

Quintiliani, M., Andreozzi, G.B. & Graziani, G. (2006). Fe^{2+} and Fe^{3+} quantification by different approaches and fO_2 estimation for Albanian Cr-spinels. *American Mineralogist* **91**, 907-916

Renner, R. & Palacz, Z.A. (1987). Basaltic replenishment of the Rhum magma chamber: evidence from unit 14. *Journal of the Geological Society, London* **144**, 961–970.

Roeder, P.L.& Campbell, I.H. (1985). The Effect of Postcumulus Reactions on Composition of Chrome-spinels from the Jimberlana Intrusion. *Journal of Petrology* **26**, 763–786.

Scowen, P.A.H., Roeder, P.L. & Helz, R.T. (1991). Requilibration of chromite within Kiliauea Iki lava lake, Hawaii. *Contributions to Mineralogy and Petrology* **107**, 8–20.

Spandler, C., Mavrogenes, J. & Arculus, R. (2005). Origin of chromitites in layered intrusions: Evidence from chromite-hosted melt inclusions from the Stillwater Complex. *Geology* **33**, 893–896

Sparks, R.S.J., Huppert, H.E., Kerr, R.C., McKenzie, D.P. & Tait, S.R. (1985). Postcumulus processes in layered intrusions. *Geological Magazine* **122**, 555–568

Tait, S.R. (1985). Fluid dynamic and geochemical evolution of the Cyclic Unit 10: Rhum intrusion. *Geological Magazine* **122**, 469–484

Tepley, F.J. III. & Davidson, J.P. (2003). Mineral-scale Sr-isotope constraints on magma evolution and chamber dynamics in the Rum Layered Intrusion, Scotland. *Contributions to Mineralogy and Petrology* **145**, 628–641

Upton, B.G.J., Scovgaard, A.C., McClurg, J., Kirstein, L., Cheadle, M., Emeleus, C.H., Wadsworth, W.J. & Fallick, A.E. (2002). Picritic magmas and the Rum ultramafic complex, Scotland. *Geological Magazine* **139**, 437–452

Veksler, I.V., Reid, D.L., Dulski, P., Jakob, K.K., Schannor, M., Hecht, L. & Trumbull, R.B. Electrochemical Processes in a Crystal Mush: Cyclic Units in the Upper Critical Zone of the Bushveld Complex, South Africa. *Journal of Petrology* **56**, 1229–1250.

Vigneresse, J.L., Barbey, P. & Cuney, M. (1996). Rheological Transitions During Partial Melting and Crystallization with Application to Felsic Magma Segregation and Transfer. *Journal of Petrology* **37**, 1579–1600.

Volker, J.A, & Upton, B.G.J. (1990). The structure and petrogenesis of the Trallval and Ruinsival areas of the Rhum ultrabasic complex. *Transactions of the Royal Society of Edinburgh: Earth Sciences* **81**, 69–88.

Voordouw, R., Gutzmer, J., Beukes, N.J. (2009). Intrusive origin for Upper Group (UG1, UG2) stratiform chromitite seams in the Dwars River area, Bushveld Complex, South Africa. *Contributions to Mineralogy and Petrology* **97**, 75–94

Vukmanovic, Z., Barnes, S.J., Reddy, S.M., Godel, B. & Fiorentini, M.L. (2013). Morphology and microstructure of chromite crystals in chromitites from the Merensky Reef (Bushveld Complex, South Africa). *Contributions to Mineralogy and Petrology* **165**, 1031–1050

Wadsworth, W.J. (1961). The layered ultrabasic rocks of south-west Rhum, Inner Hebrides. *Philosophical Transactions of the Royal Society of London. Series* B **244**, 21–64

Wager, L.R., Brown, G.M. & Wadsworth, W.J. (1960). Types of Igneous Cumulates. Journal of Petrology **1**, 73–85

Wager, L.R. & Deer, W.A. (1939) Geological investigations in East Greenland. Part III. The petrology of the Skaergaard intrusion, Kangerdlugssuak, east Greenland. *Meddelelser om Grønland*, **105**, 1-352

Welsch, B., Hammer, J. & Hellebrand, E. (2014). Phosphorus zoning reveals dendritic architecture of olivine. *Geology* **42**, 867–870

Wijbrans, C.H., Klemme, S., Berndt, J. & Vollmer, C. (2015). Experimental determination of trace element partition coefficients between spinel and silicate melt: the influence of chemical composition and oxygen fugacity. *Contributions to Mineralogy and Petrology* **169**, 1128-1161

Worrell, L.M. (2002). The Origin of Igneous Cumulates: Integrated Studies of Peridotites from the Western Layered Series of the Rum Layered Intrusion. *Unpublished PhD Thesis, University of Liverpool*

Figure 1. (a) Location map of the Isle of Rum in Scotland. (b) Location of the Rum Layered Suite with the Eastern Layered Intrusion (ELI) highlighted in blue, and the Western Layered Intrusion (WLI) in green, CI = Central Intrusion (c) Geological map (after Emeleus, 1994) of the Eastern Layered Intrusion showing the position of Unit 10 (black bar) and a schematic log showing the major boundary chromitites (black bands, modified after Emeleus *et al*., 1996).

Figure 2. Simplified graphic logs through the Unit 10 peridotite with the four logged sections indicated on the ELI map (red numbered dots). Harrisitic peridotite layers can potentially be correlated (medium green bands) across the four localities in packages of similar stratigraphic position and layer characteristics. Note the abundance of thinner layers in location and 4 compared to 1, with some harrisite layers thickening towards location 1 (with distance from the Long Loch Fault feeder zone).

Figure 3. Selected stratigraphic sections of the Unit 10 peridotite referenced in Figure 2. (a) Base of the Unit 10 peridotite with troctolite autoliths incorporated into the granular-textured peridotite. Thick harrisite layer also contains a granular-textured peridotite lenses, and variable olivine morphologies. (b) Tapering harrisite layer with associated Cr-spinel seams also featured in Figure 5. Cr-spinel seams occur commonly in proximity to the tapering harrisite (c) Harrisite apophyses and layer deformation with a harrisite layer at the source-proximal Barkeval locality, also shown in Figure 4d. (d) Variable grain sizes of granular-textured peridotite layers with well-defined Cr-spinel seam above coarse granular-textured peridotite. Note the fining of olivine just above the seam also seen in Figure 7d. (e) Upper and lower peridotite contact. Pyroxene increase with height and rare tapering harrisite layers with associated external olivine grain size reduction. (f) Top of the UP, with pyroxene rich harrisite layers and bounding pegmatite between the peridotite and feldspathic cumulate. See Electronic Appendix 1 for full high resolution graphic logs, with location grid references and stratigraphic sample locations used in this study.

Figure 4. Field features of the Unit 10 lower peridotite. (a) Troctolite autolith (outlined) in granular-textured peridotite ~ 2m from the Unit 9–10 boundary. Note the irregular shape with layering parallel

to host peridotite. (b) Close of the edge of the troctolite autolith in ‘a’ with chromitite clot outlined between the two lithologies. (c) Clearly defined Cr-spinel seam on the top surface of a very coarse granular-textured peridotite, with overlying very fine grained low intercumulus volume granular-textured peridotite. Note the loop-like culmination in the centre of the Cr-spinel seam outlined and also chain-textured seam ~2 cm above well-defined seam (arrowed). (d) Broken Cr-spinel seam (outlined) above harrisite with minor upwelling of harrisite between the break in the seam. (e) Multiple, cm-thick Cr-spinel seams (arrowed) in varying lithologies. The uppermost and lowermost arrowed seams occur above and below a harrisite, respectively, with the central seams occurring in granular-textured peridotite. (f) Boundary-type Cr-spinel seam (outlined) at the base of high intercumulus harrisite. (g) Clinopyroxene-oikocrystic peridotite from the upper peridotite. Note the high abundance of rounded–elongated dark-green diopside oikocrysts. (h) Vertical oriented ‘hopper-harrisitic’ peridotite from the upper peridotite (outlined). Note the large, rounded, dark olivine crystals in the hopper-harrisite. Way up indicated by arrow.

Figure 5. Harrisite features of the lower peridotite. (a) Highly skeletal olivine crystals in harrisite layer up to several cm long. (b) Internal textural variation of harrisite layer. Coarse skeletal patch within finer skeletal harrisite layer. (c) High amplitude harrisite apophyses from the Barkeval locality protruding into well-layered granular-textured peridotite above. Note the brittle-like disturbance of well-layered peridotite left of the apophyses, now dipping variably from the layers above. (d) Low amplitude irregularities in the upper surface of harrisite layer around Hallival. (e) Tapering harrisite layer around Hallival (outlined) with irregular upper surface, discontinuous Cr-spinel seams along the base including chain-textured Cr-spinel seam which continues into granular-textured peridotite to the left as the harrisite terminates.

Figure 5 continued. Black outlines in (e) show locations of (f) chain-textured Cr-spinel seam in granular-textured peridotite ahead of tapering harrisite layer, (g) irregular upper contacts of harrisite at layer toe. Note also the variation in intercumulus abundance within the harrisite (outlined) and granular-textured peridotite around, and (h) centimetre-sized skeletal olivine within harrisite layer.

Figure 6. Petrography of the Unit 10 peridotite. (a) Optical zonation of intercumulus plagioclase crystals (examples arrowed) several mm above a boundary-type Cr-spinel seam from the lower peridotite. Note also the preferential placement of Cr-spinel at plagioclase/plagioclase grain boundaries in patches of finer-grained intercumulus plagioclase. (b) Oscillatory zoning in plagioclase oikocryst from a diffuse Cr-spinel seams of the lower peridotite. (c) Strong layer parallel foliation in harrisite from the lower peridotite. (d) Well-defined Cr-spinel seam above very coarse grained–harrisite. A reduction in intercumulus volume is observed immediately above the seam, and the development of high angle triple grain boundaries between granular olivine crystals (arrowed). (e) Example of 'chain-textured' Cr-spinel seam with cumulus olivine crystals within the limits of the seam. The olivine crystals have many (potentially deep) embayments now occupied by Cr-spinel (arrowed). (f) Reflective-light photomicrograph showing multiple high reflectivity sulphide crystals closely associated with Cr-spinel from a very diffuse seam in the lower peridotite. (g) Reflective-light photomicrograph of various Cu-Ni sulphides with magnetite attached to Cr-spinel. (h) Typical clinopyroxene-oikocrystic peridotite from the upper peridotite with large, clinopyroxene crystals occupying significant intercumulus volume. Note also the larger hopper olivine grain in the top centre of the image.

Figure 7. QEMSCAN® image of well-defined Cr-spinel seam featured in Figure 4f and 6d, adapted from O'Driscoll *et al*. (2014). White circles indicate the position of detected PGM grains, with white arrows at the base indicating PGMs just beyond the view of the image. Red arrows at the base indicate the position of electrum (Au-Ag alloy) grains just beyond the image. Note also the 'patchy' zonation of intercumulus plagioclase (varied blue shade) highlighted in the white boxes.

Figure 8. QEMSCAN® image of diffuse, PGM-rich, Cr-spinel seam (Sample U10I) from the LP, with close up image of boxed area highlighting the abundance of sulphide minerals. Black circles indicate the position of PGM grains, with BSE images of particular PGM grains highlighted by the arrowed circle. Note the unusual presence of clinopyroxene in long vertically oriented structures, and sharp grain size change of olivine in the top of the image.

Figure 9. Crystal size distribution diagrams of the sixteen Cr-spinel seams analysed in this study, separated into the four seam groups discussed in the text. The Unit 11-12 main seam and two peridotite hosted Cr-spinel seams from the Unit 12 peridotite in red (O'Driscoll *et al*., 2010) are included for comparison. Red circles denote CSD bins with significant errors. All error data can be found in Electronic Appendix 2.

Figure 10. Crystal size distribution derivative diagrams for Cr-spinel seams analysed in this study. See text for explanation.

Figure 11. Selected Fenner diagrams for whole rock analyses of Cr_2O_3, FeO_t, and Al_2O_3 for peridotites in Unit 10. ''M9'' analysed as part of this study is the same picritic dyke as discussed in Upton *et al*. (2002). Note the moderate segregation of harrisite and granular-textured peridotite types.

Figure 12. Ni (ppm) versus Forserite abundance (mol. %) of olivines from the Unit 10 peridotite. Note the significant overlap of all peridotite types of the lower peridotite. Upper peridotite olivine has lower Fo-values than lower peridotite olivines.

Figure 13. (a) Cr# vs Mg# diagram for Unit 10 Cr-spinel data analyses from Rum, divided into host peridotite lithology, compared with other peridotite-hosted Cr-spinels from the RLS, 1 = Unit 10 (this study), 2 = Unit 9, disseminated Cr-spinel (Holness *et al*., 2007b), 3 = Unit 12 'supra-seams' (O'Driscoll *et al*., 2010), 4 = ''M9'' picrite disseminated Cr-spinel (Upton *et al*., 2002; O'Driscoll *et al*., 2010). (b) Cr-spinel trivalent cation ternary diagram (Al^{3+} - Cr^{3+} - Fe^{3+}) for spinels from the Unit 10 peridotite (1). Peridotite hosted Cr-spinel from other sections of the RLS are included for comparison (as above). These all cluster relatively close to the Unit 10 data, with the Unit 12 seams being the most aluminous. Note the Fe^{3+} and Al^{3+} variation between Cr-spinel within seams, and within the surrounding peridotite. See text for discussion.

Figure 14. Chemical traverses of Cr#[$Cr^{3+}/(Cr^{3+}+Al^{3+})$] and TiO_2 wt. % across a Cr-spinel seam from the lower peridotite, with harrisite above the seam and granular-textured peridotite beneath it. A decrease in Cr# corresponds to an increase in Al^{3+}. The position of the seam on each sample has been highlighted for clarity. An increase in TiO_2 with a decrease in Cr# is typically occurs in Cr-spinel

outside the limits of the seam. Additional traverses can be found in Electronic Appendix 5.Figure 15. Mineral composition element maps from the lower peridotite (three samples a–c, see text for detailed location description) showing varied intercumulus plagioclase zonation in Na, and patchy zoning of Cr in a clinopyroxene oikocryst from the upper peridotite (d). (a) Oscillatory zoning in intercumulus plagioclase. (b) Reverse zoning of intercumulus plagioclase within Cr-spinel seam. Note the lack of Cr-spinel occurring on Na-rich cores. (c) Normal zoning of intercumulus plagioclase with irregular, jagged low-Na cores ~3 mm above a Cr-spinel seam. An content variation between zones of approximately 7–12 An units (Hepworth, unpublished data). The dark blue intercumulus phase is clinopyroxene. (d) see above.

Figure 16. Pseudo-ternary phase diagram for the system olivine-plagioclase-clinopyroxene + spinel denoted Fo-An-Di-Sp, respectively, after Morse (1980), depicting the reactions involved in Cr-spinel petrogenesis for the Unit 10 peridotite, as discussed in the text.

Figure 17. Qualitative illustration of tensile strength of a mush with increasing crystallinity, adapted from Marsh (2002). Zones of likely (and unlikely) tearing highlighted. See text for discussion.

Figure 18. Conceptual model for magmatic processes operating during the incremental construction of the Unit 10 peridotite, with insets illustrating processes in Cr-spinel seam petrogenesis (a–c) Shearing caused by sagging of the mush causes hot tearing, creating linear zones of weakness which is infiltrated by picritic magma. Foliation may be produced here. Picrite intrudes the tear, causing preferential dissolution of plagioclase increasing permeability of the mush as it dissolves plagioclase with minor olivine (e.g. Quick, 1981; Kelemen, 1990). The dissolution reaction produces a hybrid Cr-spinel saturated liquid (blue) that will migrate through the tear, crystallising abundant Cr-spinel *in situ*. If no sill forms, a granular-type seam will form from the Cr-spinel saturated liquid *in situ*, e.g. (b). If the picrite continues to flow within the tear it will inflate into a sill, forming boundary-type Cr-spinel seams, e.g. (c). Continued flow within a rapidly crystallising harrisite sill will produce harrisite-type seams from the dissolution of intercumulus plagioclase within harrisite. These seams will be locally unconstrained by shear and are not necessarily layer-parallel. (d) Displacement and

assimilation processes of host mineralogy/liquid on injection of picritic magma into the crystal mush producing variable plagioclase zoning types. Reverse zoning formed during assimilation of pre-existing plagioclase, with precipitation of high-anorthite rims of plagioclase at the site of Cr-spinel formation. Above the sill, normal zoning forming by the displacement of host liquid on intrusive replenishment of picrite, producing low-anorthite rims on crystallising plagioclase.

Figure 19. Whole rock $^{87}Sr/^{86}Sr$ ratios through the Unit 10 peridotite (from Palacz & Tait, 1985; uncertainities smaller than symbol size), with graphical separation of the lower and upper peridotite and feldspathic cumulate based on this study. Zone of proposed partial melting arrowed (see text).

Figure 1

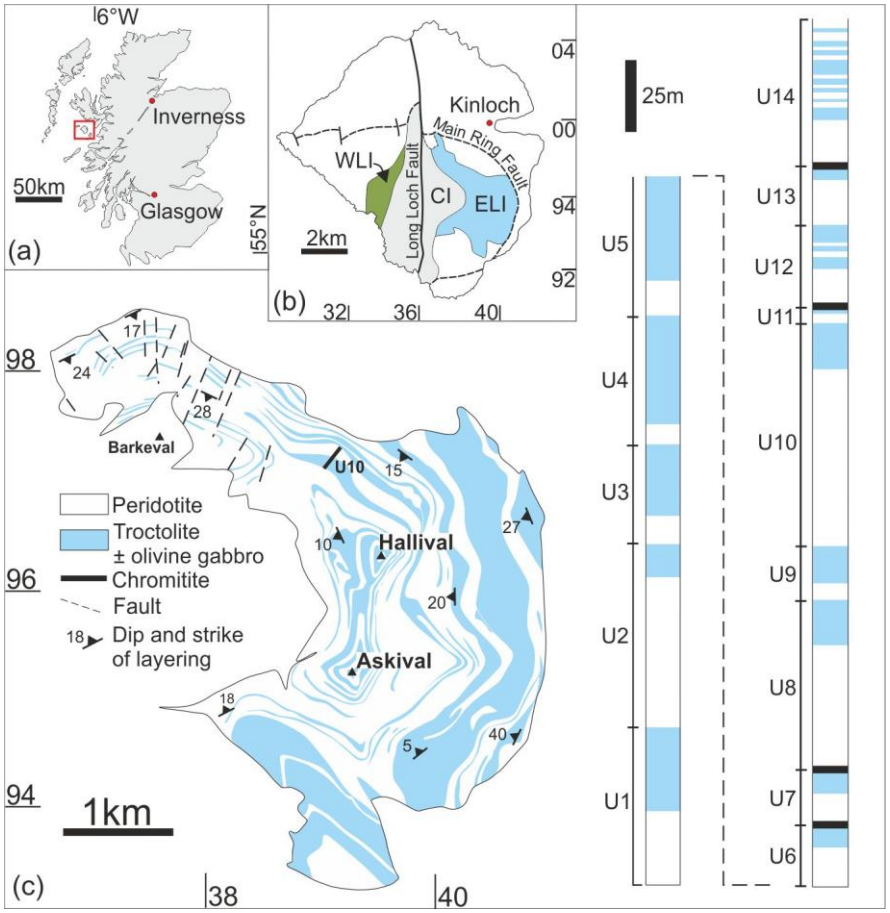
6°W
Inverness
50km
Glasgow
(a)
55°N
Kinloch
Main Ring Fault
WLI
Long Loch Fault
CI
ELI
2km
(b)
04
00
94
92
32
36
40
25m
U14
U13
U12
U11
U10
U9
U8
U7
U6
U5
U4
U3
U2
U1
98
96
94
17
24
28
Barkeval
U10
15
27
10
Hallival
20
Askival
18
5
40
Peridotite
Troctolite
± olivine gabbro
Chromitite
Fault
18
Dip and strike
of layering
1km
(c)
38
40

Figure 2

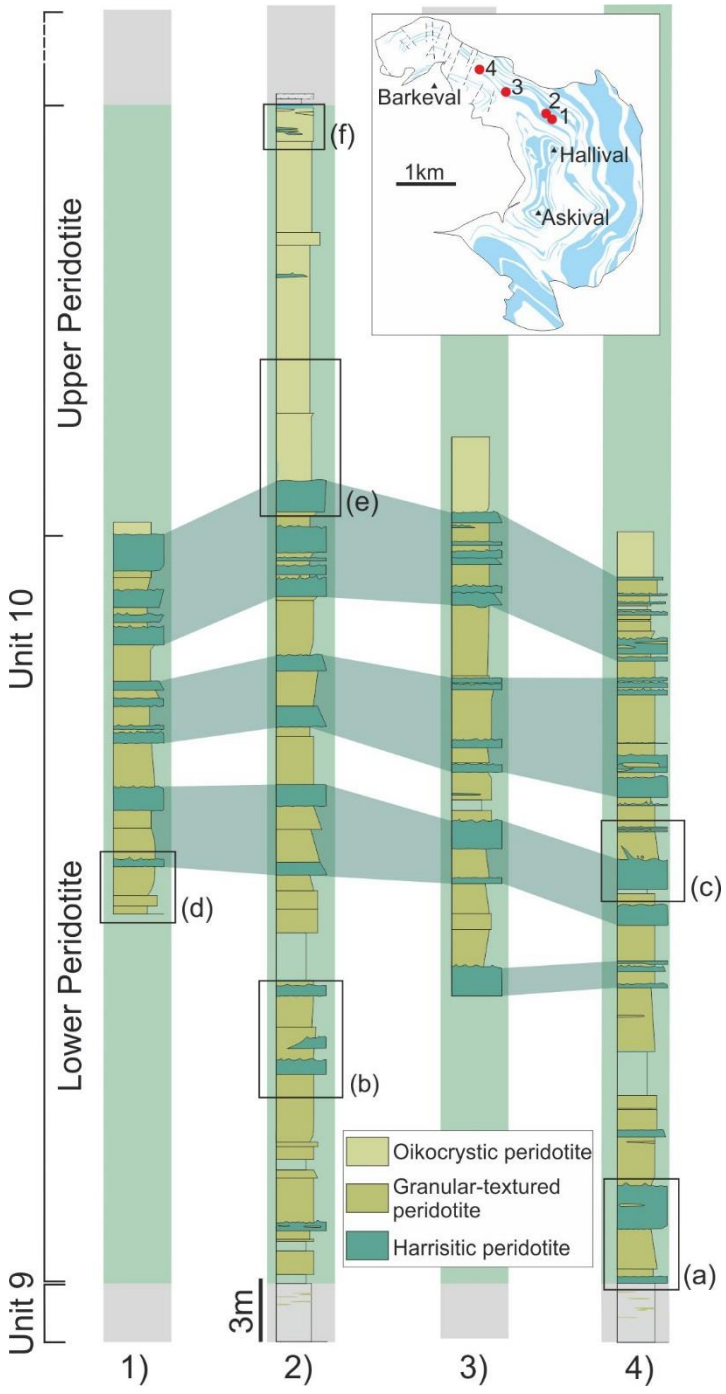
Unit 10
Upper Peridotite
Lower Peridotite
Unit 9
(f)
(e)
(d)
(b)
(c)
(a)
3m
1)
2)
3)
4)
Barkeval
Hallival
Askival
1km
Oikocrystic peridotite
Granular-textured peridotite
Harrisitic peridotite

Figure 3

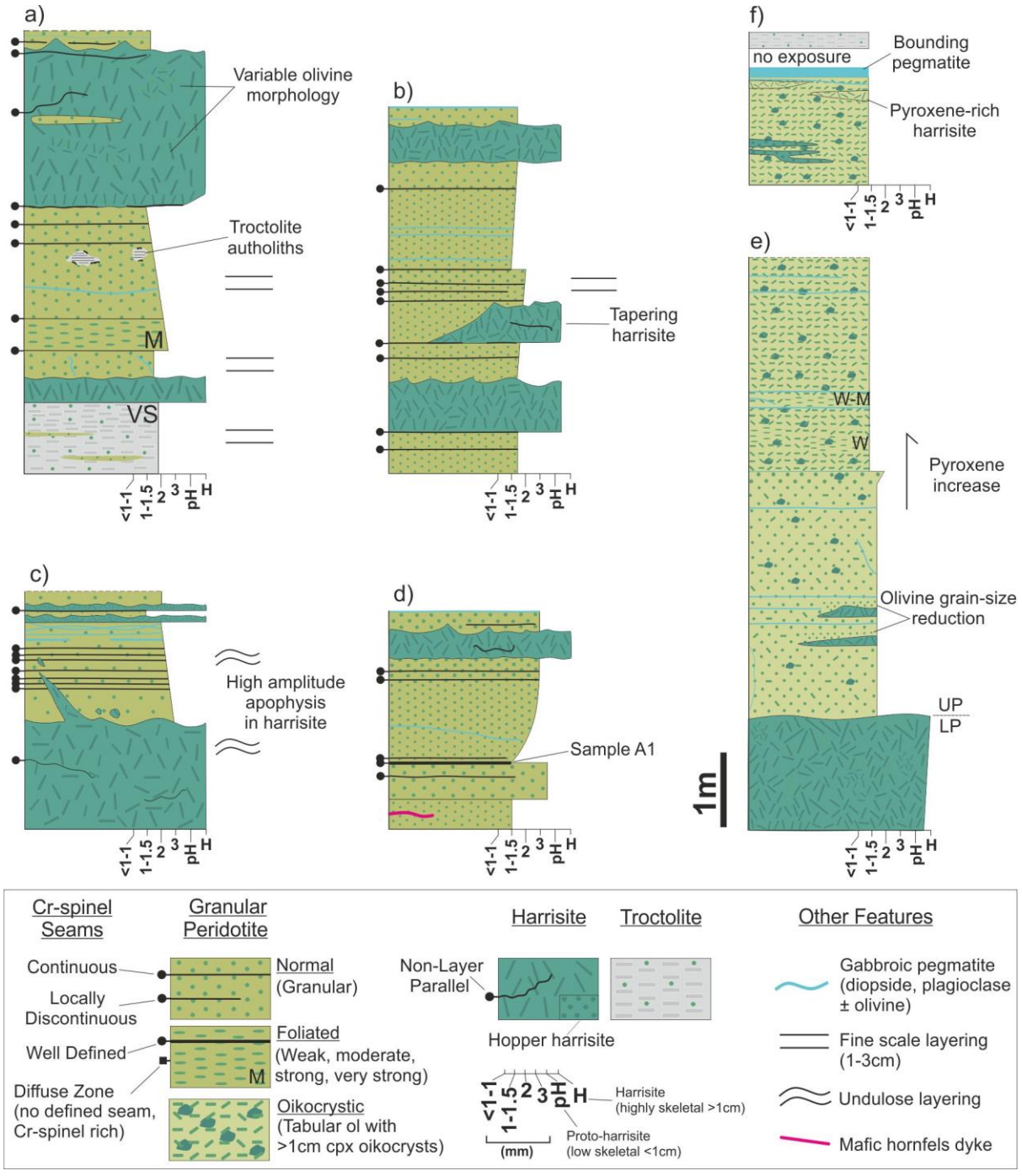
a)
Variable olivine morphology
Troctolite autholiths
M
VS
<1-1
1-1.5
2
3
pH
H
b)
Tapering harrisite
c)
High amplitude apophysis in harrisite
d)
Sample A1
f)
no exposure
Bounding pegmatite
Pyroxene-rich harrisite
e)
W-M
W
Pyroxene increase
Olivine grain-size reduction
UP
LP
1m
Cr-spinel Seams
Granular Peridotite
Continuous
Locally Discontinuous
Well Defined
Diffuse Zone (no defined seam, Cr-spinel rich)
Normal (Granular)
Foliated (Weak, moderate, strong, very strong)
Oikocrystic (Tabular ol with >1cm cpx oikocrysts)
Harrisite
Troctolite
Non-Layer Parallel
Hopper harrisite
(mm)
Harrisite (highly skeletal >1cm)
Proto-harrisite (low skeletal <1cm)
Other Features
Gabbroic pegmatite (diopside, plagioclase ± olivine)
Fine scale layering (1-3cm)
Undulose layering
Mafic hornfels dyke

Figure 4

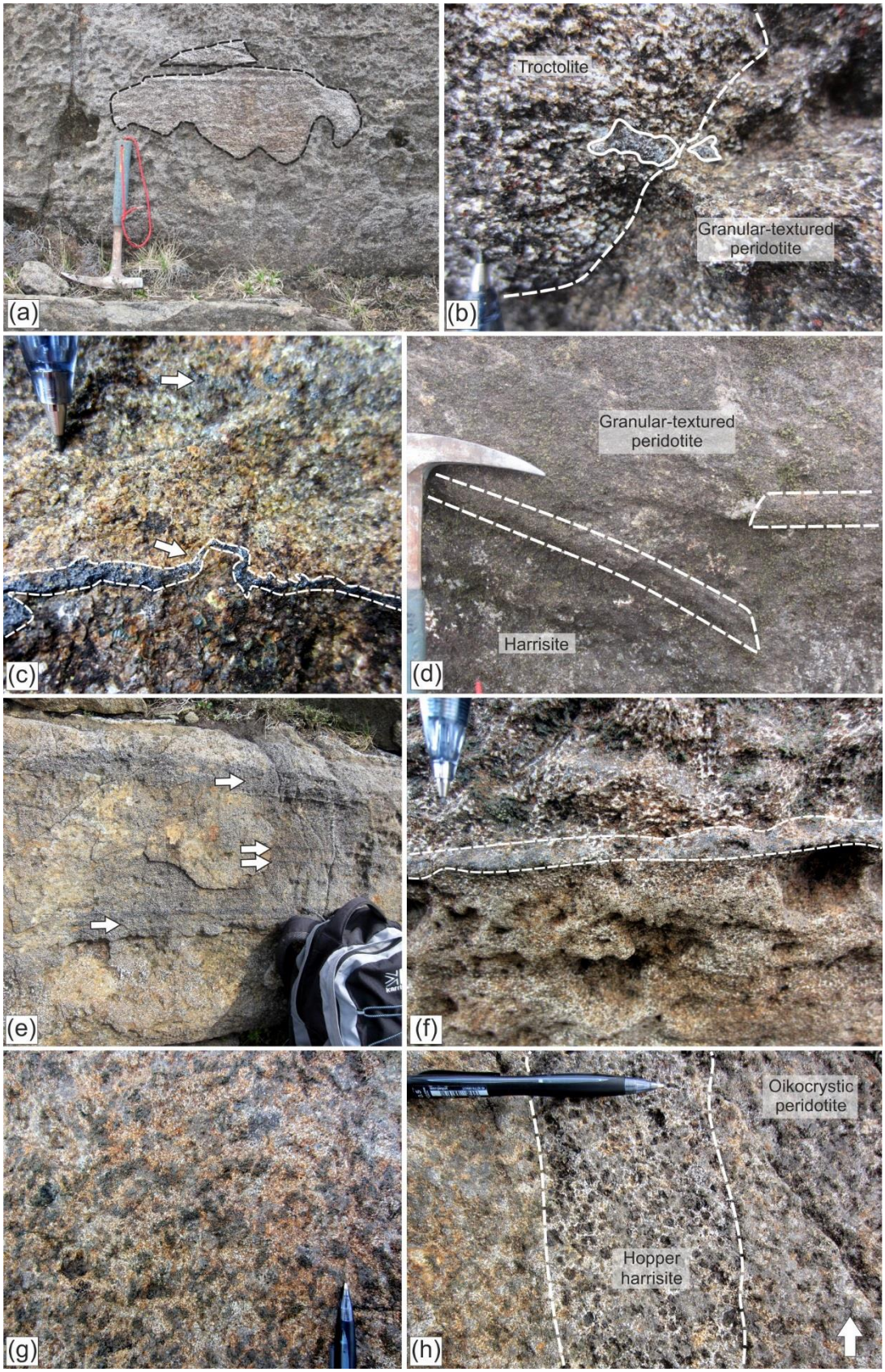
(a)
Troctolite
Granular-textured peridotite
(b)
(c)
Granular-textured peridotite
Harrisite
(d)
(e)
(f)
(g)
Oikocrystic peridotite
Hopper harrisite
(h)

Figure 5

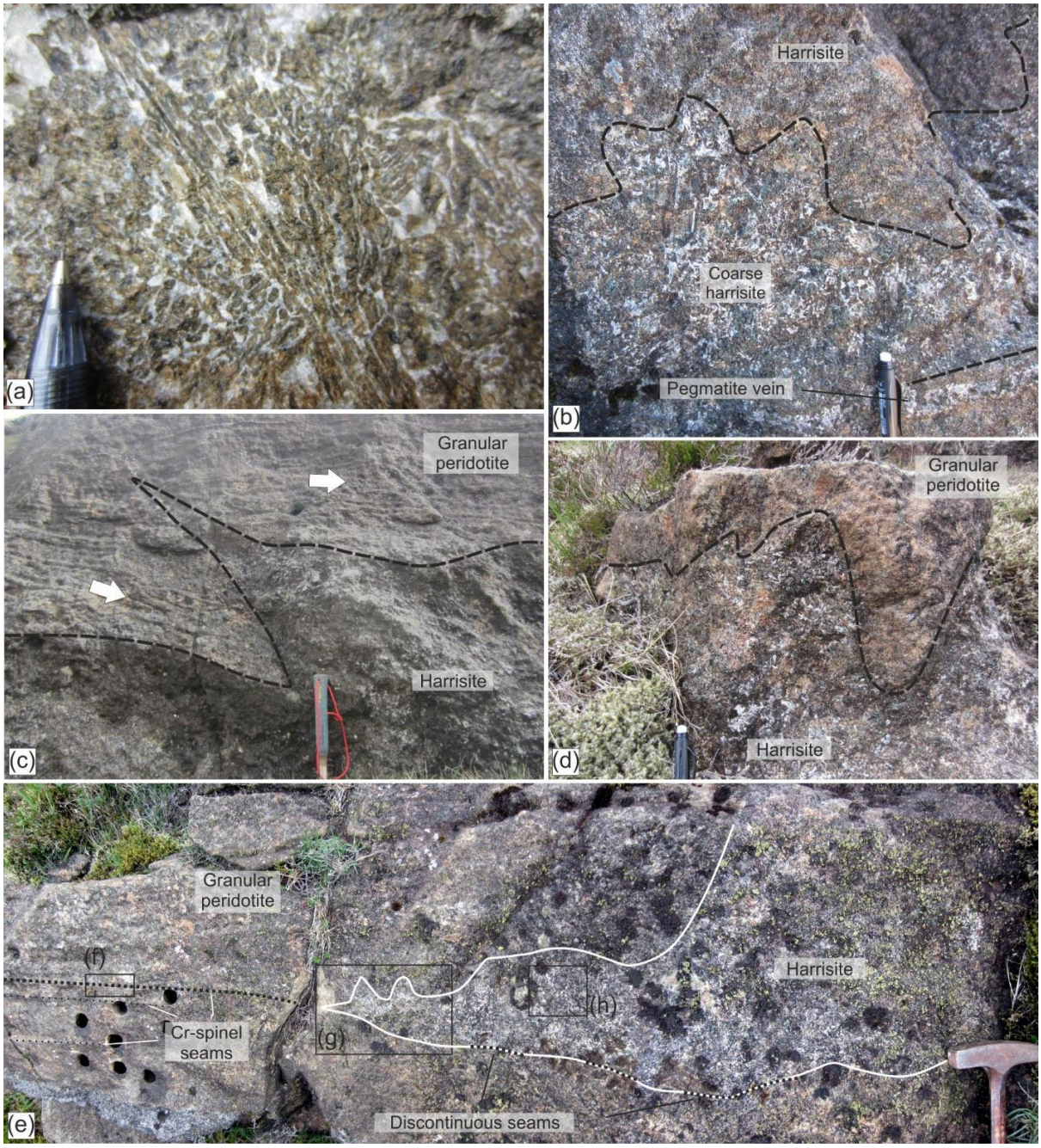
(a)
Harrisite
Coarse harrisite
Pegmatite vein
(b)
Granular peridotite
Harrisite
(c)
Granular peridotite
Harrisite
(d)
Granular peridotite
(f)
Cr-spinel seams
(g)
(h)
Harrisite
Discontinuous seams
(e)

Figure 5 continued

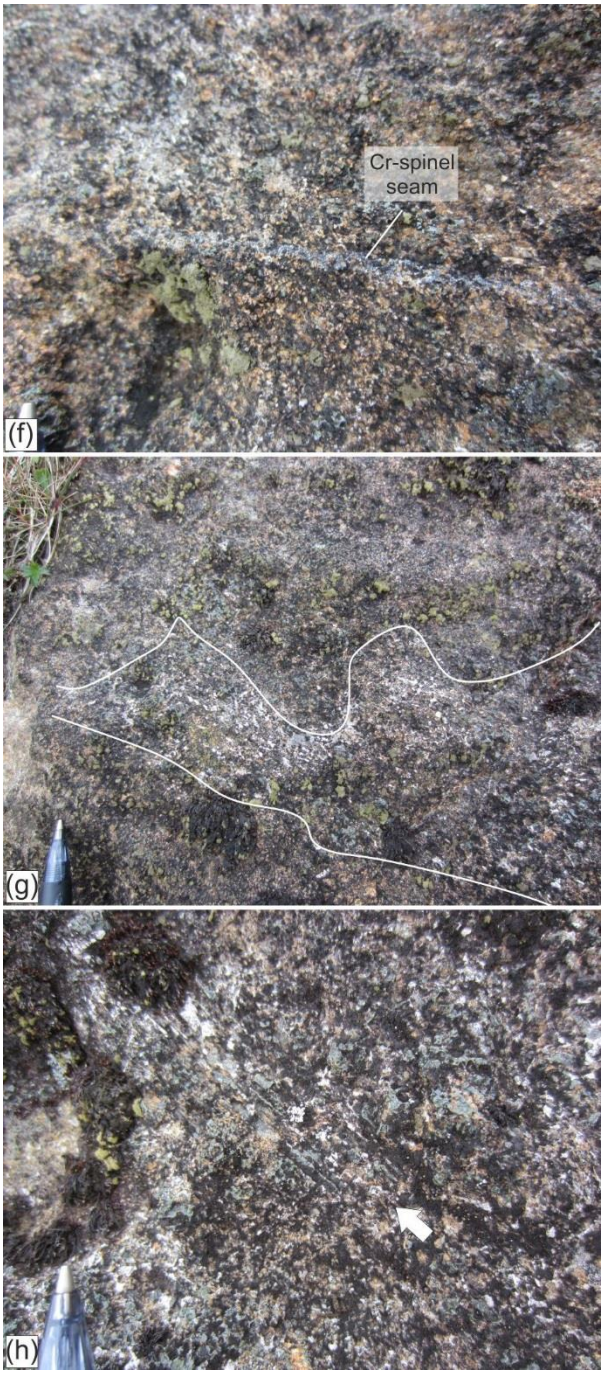

Figure 6

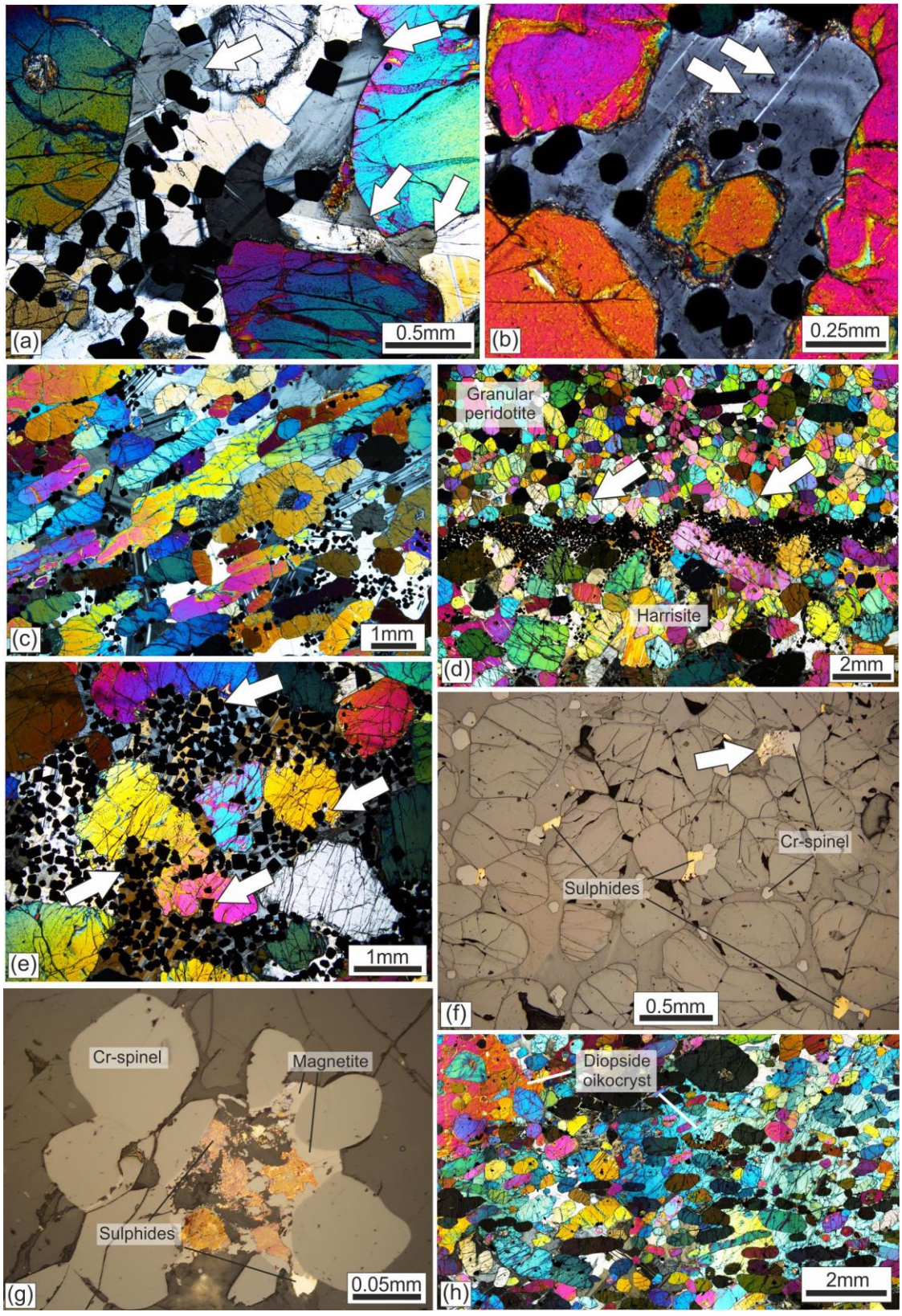
(a)
0.5mm
(b)
0.25mm
(c)
1mm
Granular peridotite
Harrisite
(d)
2mm
(e)
1mm
Cr-spinel
Sulphides
(f)
0.5mm
Cr-spinel
Magnetite
Sulphides
(g)
0.05mm
Diopside oikocryst
(h)
2mm

Figure 7

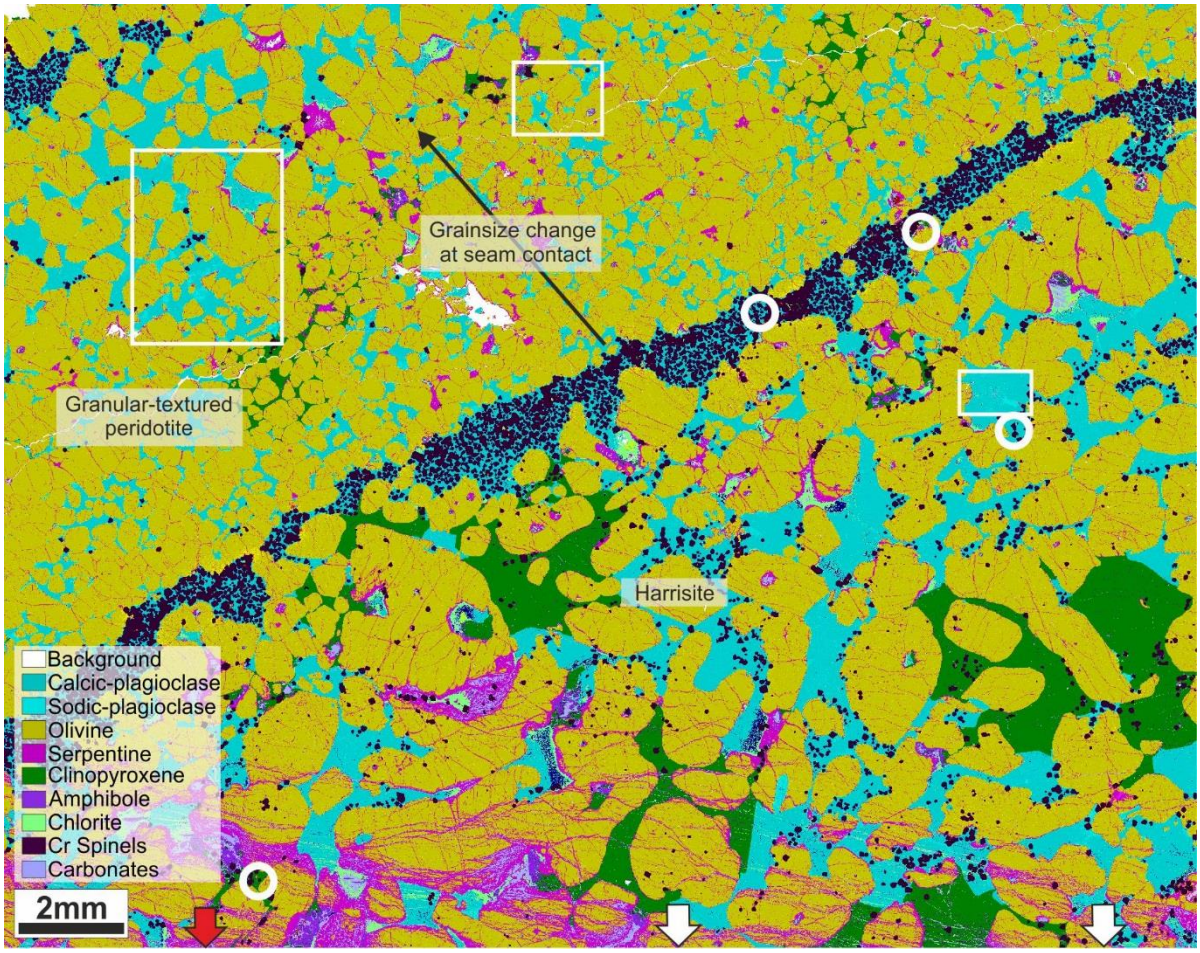
Grainsize change
at seam contact
Granular-textured
peridotite
Harrisite
Background
Calcic-plagioclase
Sodic-plagioclase
Olivine
Serpentine
Clinopyroxene
Amphibole
Chlorite
Cr Spinels
Carbonates
2mm

Figure 8

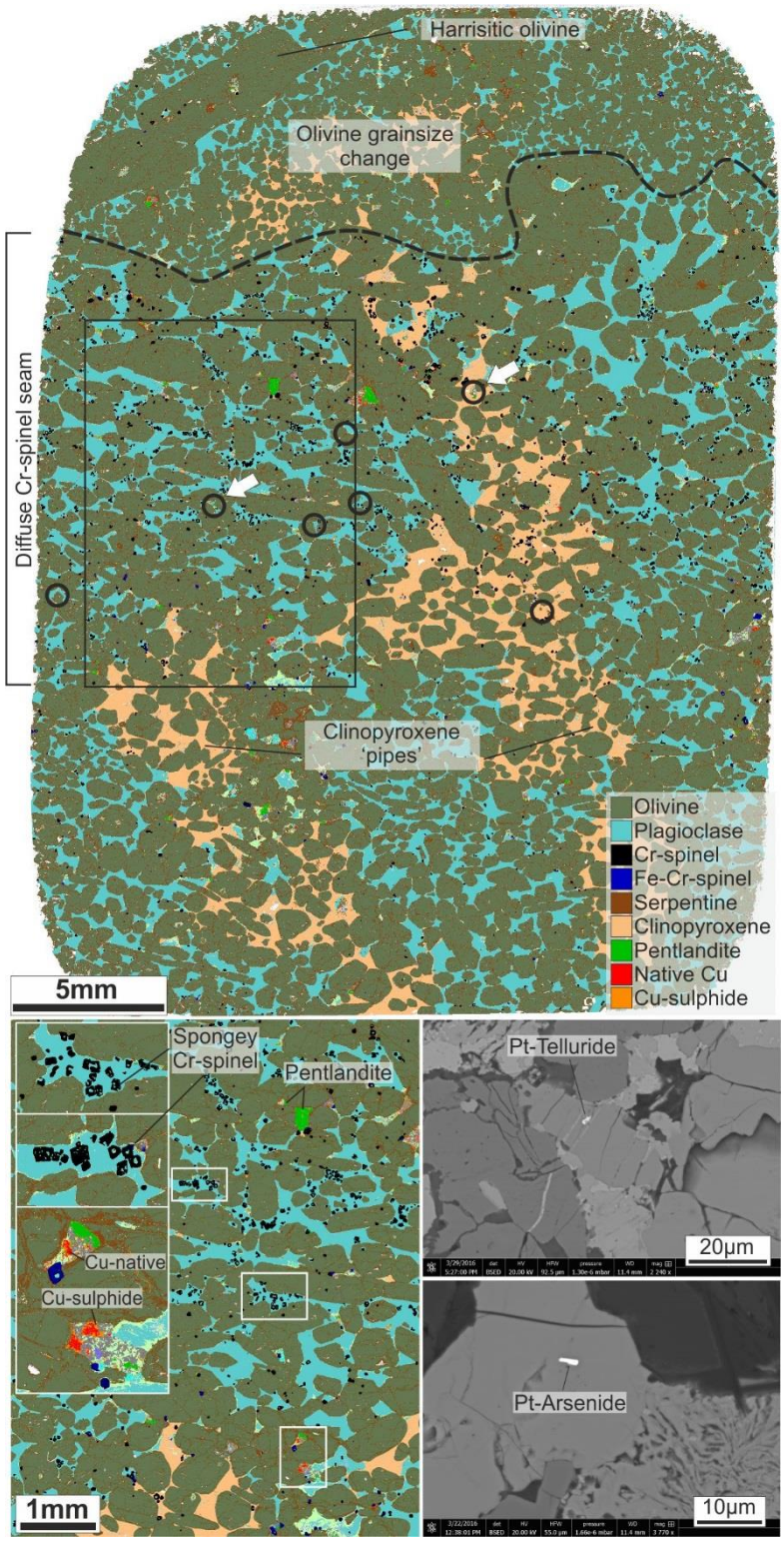
Harrisitic olivine
Olivine grainsize change
Diffuse Cr-spinel seam
Clinopyroxene 'pipes'
Olivine
Plagioclase
Cr-spinel
Fe-Cr-spinel
Serpentine
Clinopyroxene
Pentlandite
Native Cu
Cu-sulphide
5mm
Spongey Cr-spinel
Pentlandite
Cu-native
Cu-sulphide
1mm
Pt-Telluride
20µm
Pt-Arsenide
10µm

Figure 9

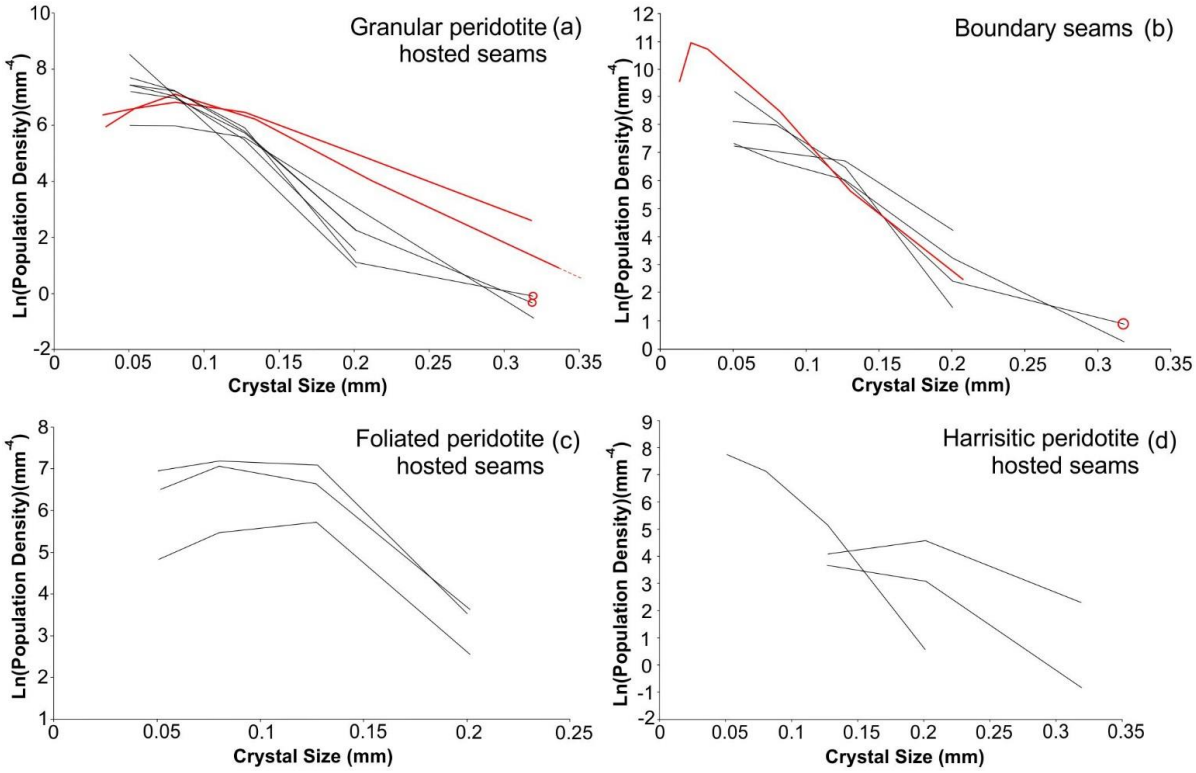
Granular peridotite (a)
hosted seams
Boundary seams (b)
Foliated peridotite (c)
hosted seams
Harrisitic peridotite (d)
hosted seams
Ln(Population Density)(mm-4)
Crystal Size (mm)

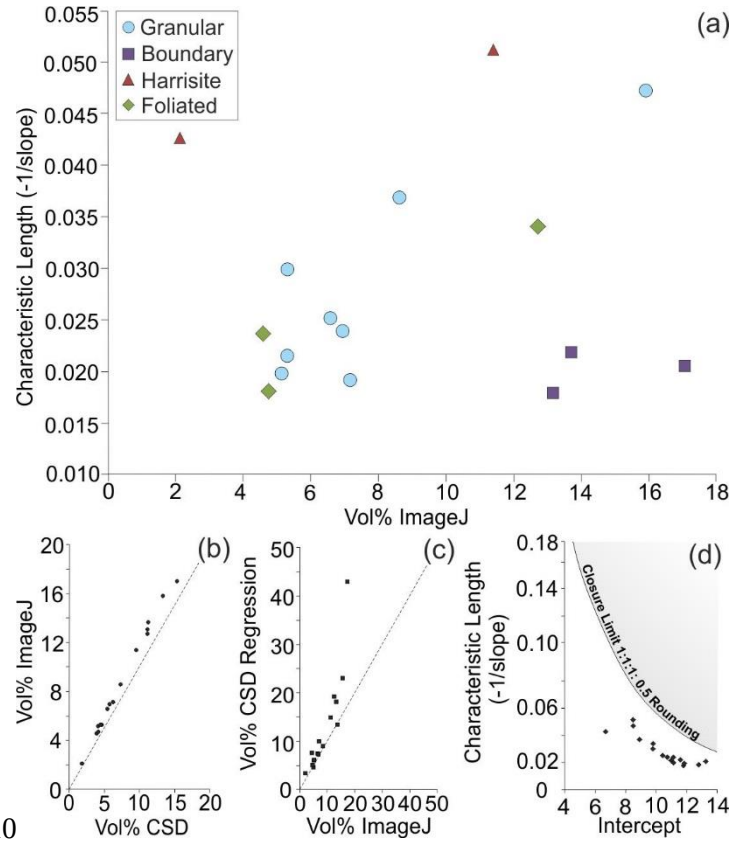
(a)
Granular
Boundary
Harrisite
Foliated
Characteristic Length (-1/slope)
Vol% ImageJ
(b)
Vol% ImageJ
Vol% CSD
(c)
Vol% CSD Regression
Vol% ImageJ
(d)
Characteristic Length (-1/slope)
Closure Limit 1:1:1; 0.5 Rounding
Intercept

Figure 10

Figure 11

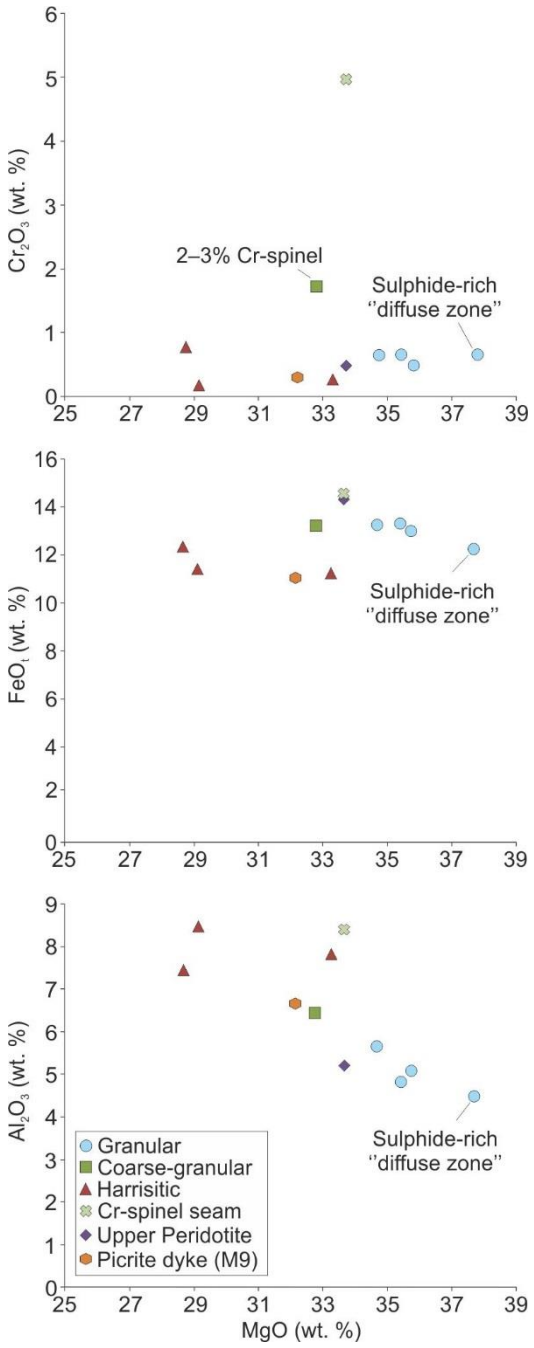
Cr_2O_3 (wt. %)
2–3% Cr-spinel
Sulphide-rich
''diffuse zone''
FeO_t (wt. %)
Sulphide-rich
''diffuse zone''
Al_2O_3 (wt. %)
Sulphide-rich
''diffuse zone''
Granular
Coarse-granular
Harrisitic
Cr-spinel seam
Upper Peridotite
Picrite dyke (M9)
MgO (wt. %)

Figure 12

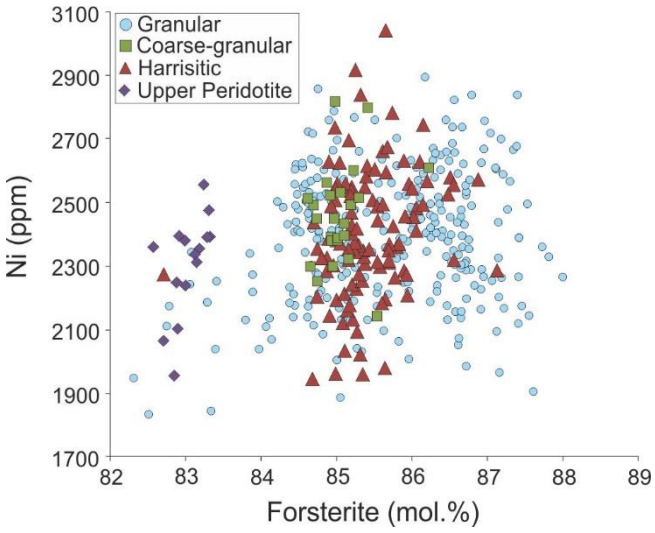
Granular
Coarse-granular
Harrisitic
Upper Peridotite
Ni (ppm)
3100
2900
2700
2500
2300
2100
1900
1700
82
83
84
85
86
87
88
89
Forsterite (mol.%)

Figure 13

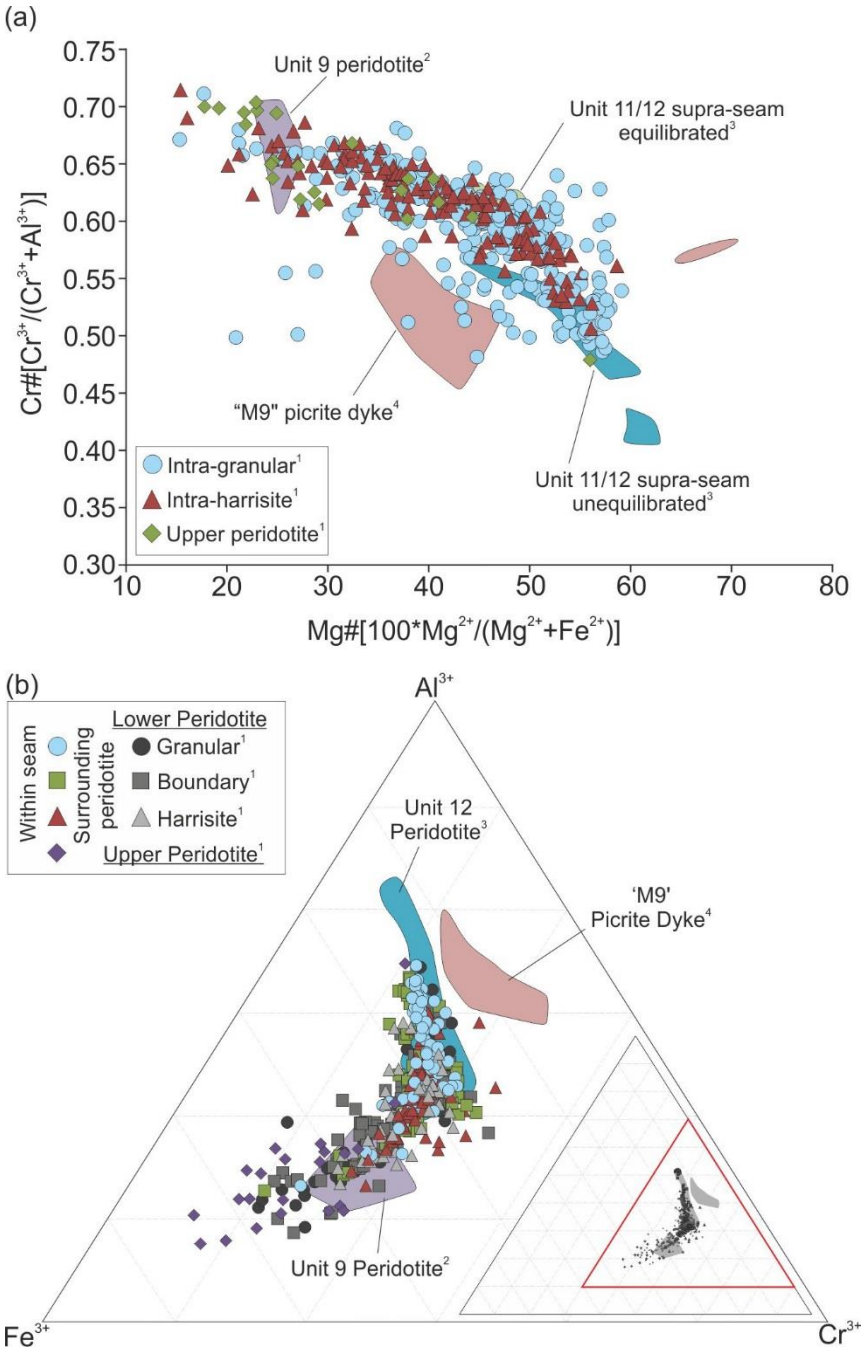
(a)
Unit 9 peridotite[2]
Unit 11/12 supra-seam equilibrated[3]
"M9" picrite dyke[4]
Unit 11/12 supra-seam unequilibrated[3]
Intra-granular[1]
Intra-harrisite[1]
Upper peridotite[1]
Cr#[Cr3+/(Cr3++Al3+)]
Mg#[100*Mg2+/(Mg2++Fe2+)]
0.75
0.70
0.65
0.60
0.55
0.50
0.45
0.40
0.35
0.30
10
20
30
40
50
60
70
80
(b)
Within seam
Surrounding peridotite
Lower Peridotite
Granular[1]
Boundary[1]
Harrisite[1]
Upper Peridotite[1]
Al3+
Unit 12 Peridotite[3]
'M9' Picrite Dyke[4]
Unit 9 Peridotite[2]
Fe3+
Cr3+

Figure 14

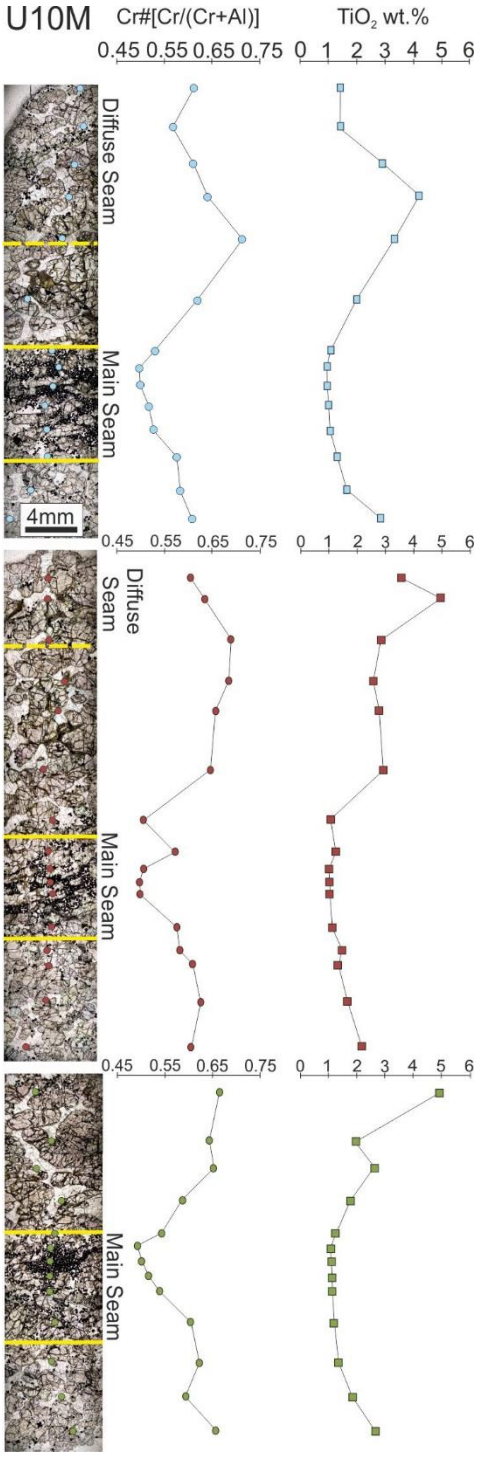
U10M
Cr#[Cr/(Cr+Al)]
TiO2 wt.%
0.45 0.55 0.65 0.75
0 1 2 3 4 5 6
Diffuse Seam
Main Seam
4mm
Diffuse Seam
Main Seam
Main Seam

Figure 15

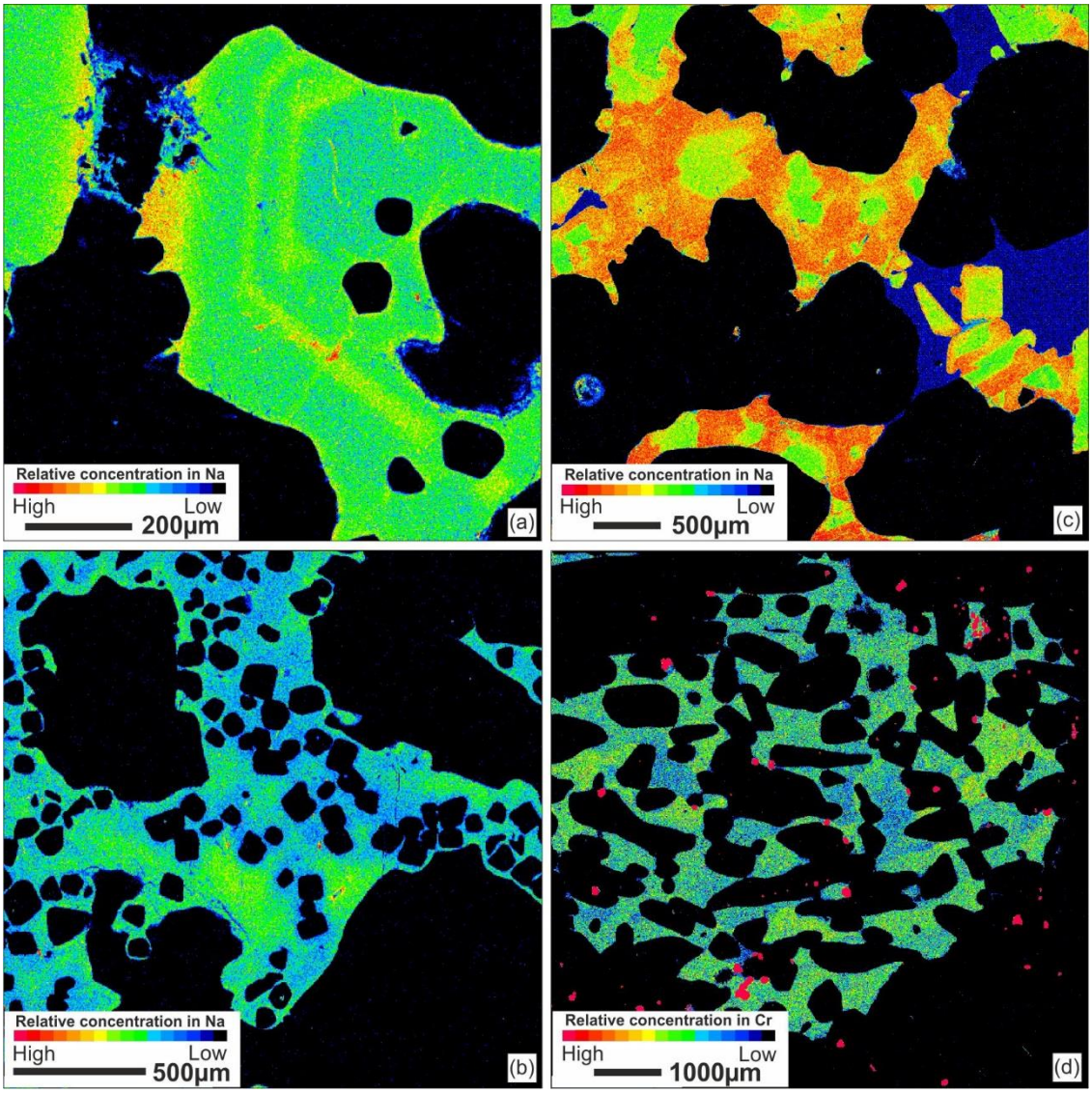
Relative concentration in Na
High
Low
200µm
(a)
Relative concentration in Na
High
Low
500µm
(c)
Relative concentration in Na
High
Low
500µm
(b)
Relative concentration in Cr
High
Low
1000µm
(d)

Figure 16

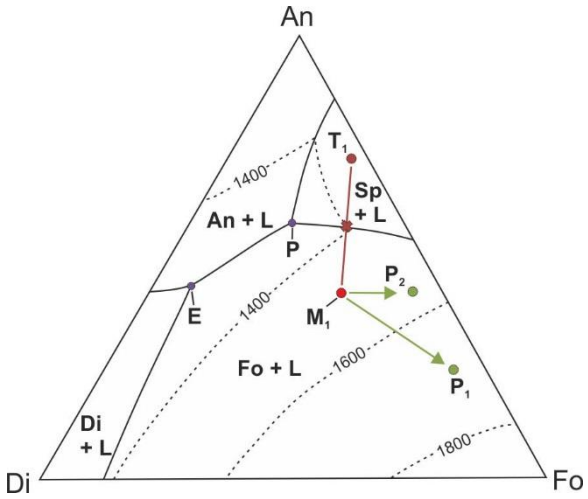

Figure 17

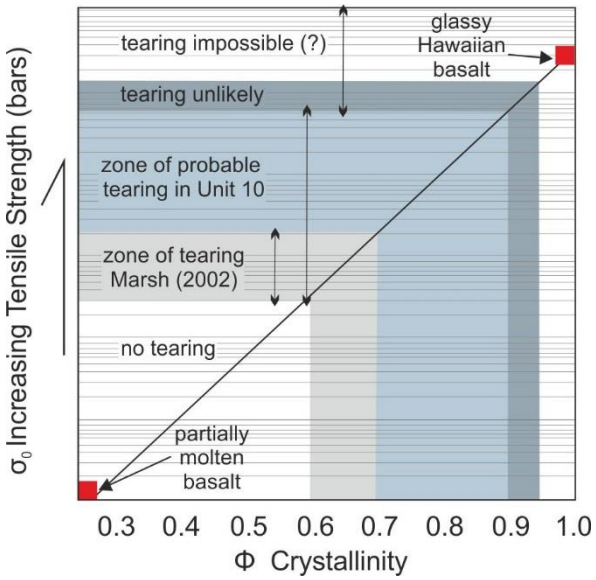
tearing impossible (?)
glassy
Hawaiian
basalt
tearing unlikely
zone of probable
tearing in Unit 10
zone of tearing
Marsh (2002)
no tearing
partially
molten
basalt
σ0 Increasing Tensile Strength (bars)
0.3
0.4
0.5
0.6
0.7
0.8
0.9
1.0
Φ Crystallinity

Figure 18

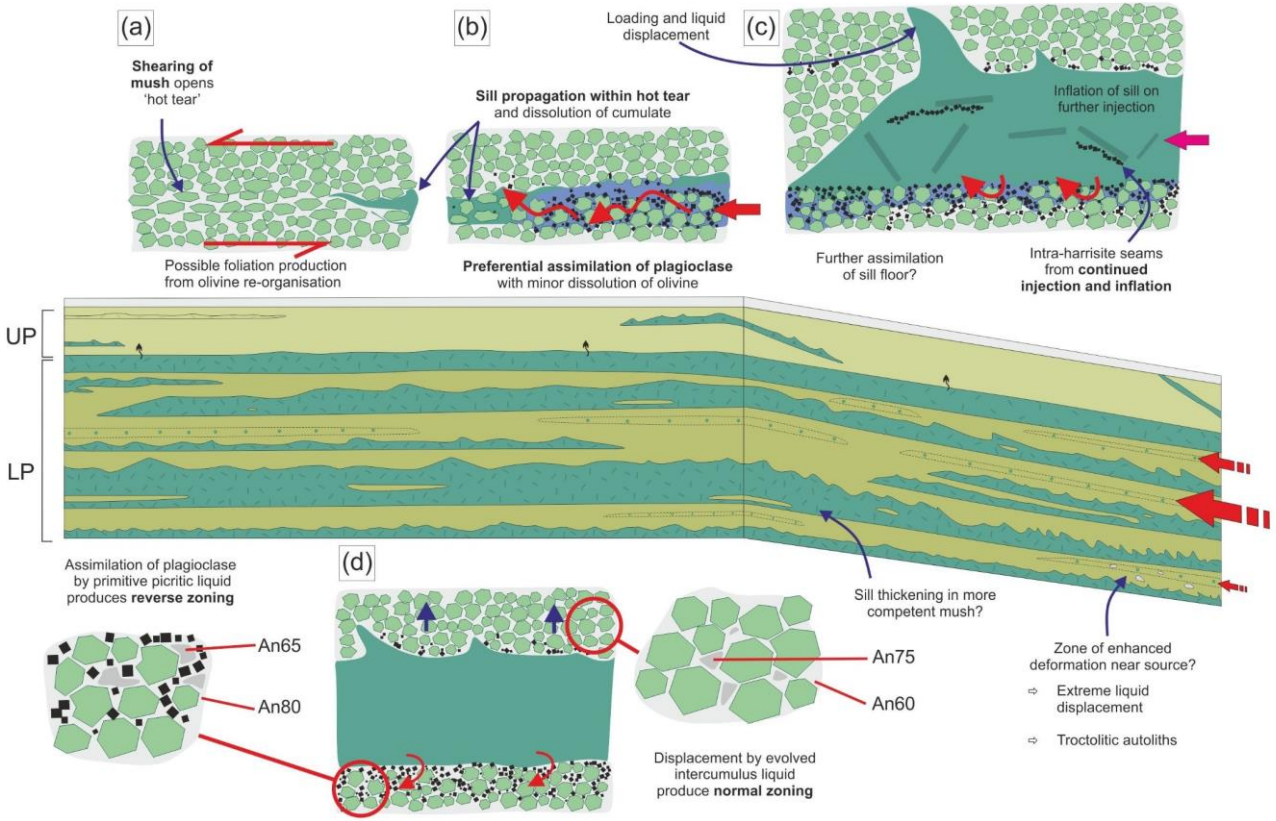
(a)
Shearing of mush opens 'hot tear'
Possible foliation production from olivine re-organisation
(b)
Sill propagation within hot tear and dissolution of cumulate
Preferential assimilation of plagioclase with minor dissolution of olivine
Loading and liquid displacement
(c)
Inflation of sill on further injection
Further assimilation of sill floor?
Intra-harrisite seams from continued injection and inflation
UP
LP
Sill thickening in more competent mush?
Zone of enhanced deformation near source?
Extreme liquid displacement
Troctolitic autoliths
Assimilation of plagioclase by primitive picritic liquid produces reverse zoning
An65
An80
(d)
An75
An60
Displacement by evolved intercumulus liquid produce normal zoning

Figure 19

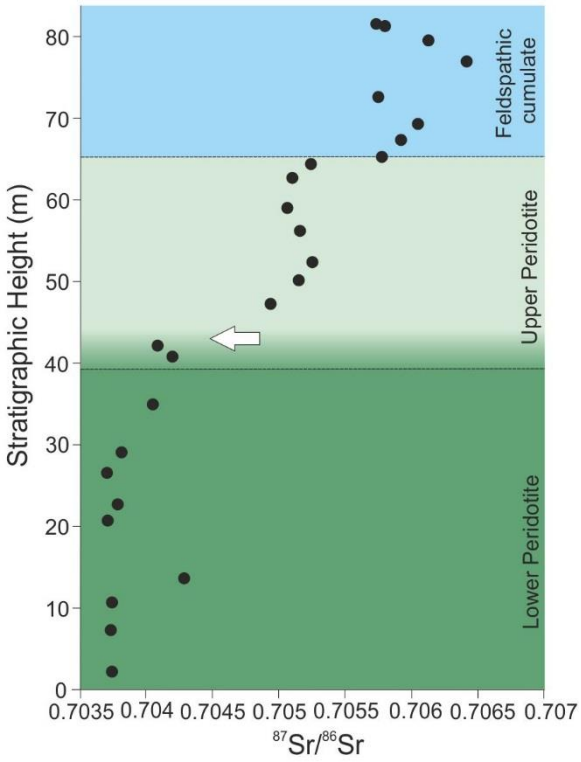
Stratigraphic Height (m)
0
10
20
30
40
50
60
70
80
0.7035 0.704 0.7045 0.705 0.7055 0.706 0.7065 0.707
$^{87}Sr/^{86}Sr$
Feldspathic cumulate
Upper Peridotite
Lower Peridotite